RSC Advances

PAPER

View Article Online
View Journal | View Issue

Open Access Article. Published on 04 February 2026. Downloaded on 2/26/2026 3:16:51 PM.
This article is licensed under a Creative Commons Attribution-NonCommercial 3.0 Unported Licence.

Check for updates

Cite this: *RSC Adv.*, 2026, **16**, 7230

Development of a chitosan-hydroxypropyl methylcellulose/nano-fluorapatite hydrogel as a novel biomaterial for enhanced post-tooth extraction bone healing in diabetic conditions

Rania A. Hanafy,[ab] Rehab M. El-Sharkawy,*[c] Eman M. Salem,[d] Nevien M. Ahmed,[e] Omnia M. Abdelfatah[d] and Wafaa Yahia Alghonemy[fg]

Received 29th September 2025
Accepted 18th January 2026

DOI: 10.1039/d5ra07408h

rsc.li/rsc-advances

A nanocomposite injectable hydrogel based on chitosan (CS), hydroxypropyl methylcellulose (HPMC), and fluorapatite nanoparticles (Nano-FA) was developed and evaluated for its bone regenerative potential following tooth extraction in diabetic rat models. Nano-FA was synthesized *via* a co-precipitation method and incorporated into a CS–HPMC hydrogel matrix to obtain a homogeneous CS–Nano-FA–HPMC composite. Forty adult male albino rats underwent bilateral extraction of the lower first molars and were randomly divided into four groups: untreated control, CS, Nano-FA, and CS–Nano-FA–HPMC. Bone healing was assessed after 2 and 6 weeks using histological, immunohistochemical, ultrastructural, histomorphometric, biochemical, and energy-dispersive X-ray analyses. The CS–Nano-FA–HPMC group exhibited significantly enhanced bone regeneration compared with the other groups, as evidenced by increased new bone formation, a higher number of entrapped osteocytes, and well-defined bone remodeling lines. Histomorphometric and statistical analyses confirmed that this group achieved the highest percentage of new bone area at both time points. In addition, inflammatory markers were markedly reduced, while osteogenic markers, including alkaline phosphatase and osteocalcin, were significantly elevated in the nanocomposite-treated group. These findings demonstrate that although CS and Nano-FA individually exhibit osteoconductive properties, their combination within a CS–Nano-FA–HPMC hydrogel provides superior regenerative performance, offering a promising strategy for enhancing bone healing under compromised diabetic conditions.

1. Introduction

In systemic conditions such as diabetes mellitus (DM), chronic inflammation, impaired angiogenesis, and delayed healing are common, with a notably higher incidence of alveolar bone atrophy after tooth extraction compared to healthy individuals.[1,2] Enhancing bone regeneration and increasing the size of the alveolar ridge are crucial for improving the safety, effectiveness, and stability of dental restorations. While autologous bones are regarded as the criterion for bone augmentation after tooth extraction in cases of bone diseases, the healing process of an allograft has proven less robust. This led to a paradigm shift towards engineered bone materials like polymers.[3]

Chitosan (CS) polymers represent a contemporary advancement in bone tissue engineering. They act as biodegradable scaffolds that support tissue proliferation and differentiation while accelerating the repair of injured tissues.[4] This functionality is attributed to its structural resemblance to glycosaminoglycans, which enable seamless interactions with collagen fibers in the extracellular matrix and promote efficient tissue regeneration and the development of biomimetic scaffolds. Histologically, it possesses osteoconductive properties, and the number of osteoblasts can be increased by applying CS to the tooth extraction socket.[5] Despite its outstanding properties as a promising biomaterial for drug delivery and wound healing, chitosan (CS) exhibits limited osteoinductive capacity, restricting its ability to regulate osteogenic differentiation effectively.[6] Bioactive components have been incorporated into CS scaffolds to address this challenge, significantly enhancing their bone-

[a]Dental Materials Department, Faculty of Dentistry, Pharos University in Alexandria, P.O. Box 37, Sidi Gaber, Alexandria, Egypt
[b]Dental Materials Department, Faculty of Dentistry, Alexandria University, Alexandria Main University Hospital, Alexandria, Egypt
[c]Chemistry Department, Faculty of Dentistry, Pharos University in Alexandria, P.O. Box 37, Sidi Gaber, Alexandria, Egypt. E-mail: rehab.mansour@pua.edu.eg; Tel: +20-1229727752
[d]Oral Biology Department, Faculty of Dentistry, Pharos University in Alexandria, P.O. Box 37, Sidi Gaber, Alexandria, Egypt
[e]Oral Biology-Biochemistry, Faculty of Dentistry, Pharos University in Alexandria, P.O. Box 37, Sidi Gaber, Alexandria, Egypt
[f]Basic Dental Sciences Department, Faculty of Dentistry, Zarqa University, Zarqa, Jordan
[g]Oral Biology Department, Faculty of Dentistry, Tanta University, Tanta, Egypt. E-mail: Wafaa_yehya@dent.tanta.edu.eg

© 2026 The Author(s). Published by the Royal Society of Chemistry

Open Access Article. Published on 04 February 2026. Downloaded on 2/26/2026 3:16:51 PM.
This article is licensed under a Creative Commons Attribution-NonCommercial 3.0 Unported Licence.

regenerative potential.[7] Hydroxyapatite nanoparticles (Nano-HA) have recently been reported to reinforce CS scaffolds, improving their mechanical performance.[8] Additionally, Nano-HA is a biocompatible candidate that has been successfully employed to enhance the alveolar ridge, sinus floor bone, and implant coating.[9–11] Furthermore, HA can be fluoridated to make FA,[12] which promotes collagen production and osseointegration.[13–15] Hydroxypropyl methylcellulose (HPMC), which has favorable physicochemical and rheological properties, was used as the paste-making agent in the formulation.[16]

Chronic inflammation is marked by a persistent and early elevation of pro-inflammatory cytokines, which disrupts the physiological cascade of tissue repair and consequently impairs or delays healing. Among these mediators, transforming growth factor-beta 1 (TGF-β1), tumor necrosis factor-alpha (TNF-α), and interleukin-1 beta (IL-1β) are particularly critical, as they actively modulate the inflammatory microenvironment and regulate key downstream signaling pathways involved in tissue regeneration.[17] Concurrently, osteogenic biomarkers such as alkaline phosphatase (ALP) and osteocalcin provide critical metrics for evaluating osteoinductive activity and determining the efficacy of therapeutic strategies aimed at enhancing bone regeneration.

Injectable chitosan-based composite hydrogels have recently attracted increasing attention owing to their biocompatibility, minimally invasive delivery, and *in situ* gelation behavior. Several studies have reported the development of injectable CS-based hydrogels for biomedical and regenerative applications, demonstrating tunable rheological, mechanical, and drug-delivery properties.[15,17] In this context, the present work contributes to this research direction by developing a CS–Nano-FA–HPMC composite hydrogel with potential applicability as an injectable or moldable scaffold system. The novelty of the present study lies in the preparation of an injectable bone-substitute paste composed of chitosan (CS), fluorapatite nanoparticles (Nano-FA), and hydroxypropyl methylcellulose (HPMC). The developed nanocomposite is designed to act as a bioactive and biocompatible matrix that enables easy clinical application, *in situ* gel formation, and improved structural stability. Nano-FA is incorporated to mimic the mineral phase of natural bone and enhance osteoconductive potential, whereas CS and HPMC contribute to the injectability, biodegradability, and mechanical integrity of the system. In addition, HPMC plays a key functional role by acting as a viscosity-enhancing polymer and a physical cross-linking component through hydrogen-bond interactions with chitosan chains. These interactions reinforce the polymeric network, improve cohesiveness, and contribute to enhanced mechanical stability and swelling behavior.

Accordingly, this study aims to evaluate the regenerative performance of the CS–Nano-FA–HPMC composite in promoting bone healing within the extraction sockets of diabetic albino rats, a model that closely represents impaired wound-healing conditions.

2. Materials & methods

All animal procedures were performed in accordance with the Guidelines for the Care and Use of Laboratory Animals of Pharos University in Alexandria and were approved by the Research Ethics Committee of the Faculty of Pharmacy, Pharos University in Alexandria (Ethical approval code: PUA-REC-012). All experimental procedures were conducted in compliance with institutional animal welfare regulations and in accordance with the ARRIVE guidelines.

2.1. Sample size calculation

Sample size estimation in this work was guided by previously reported experimental findings related to extraction socket healing in rat models treated with boron and fish oil.[18] A standardized effect size of 0.8140 was identified according to the reported primary outcome. Using this effect size, a statistical power of 80% ($\beta = 0.20$), and a significance threshold of 5% ($\alpha = 0.05$), the minimum required number of animals was calculated to be 10 per group, following standard sample size determination guidelines.[19] Subsequently, 40 male albino rats were enrolled and equally distributed across four experimental groups. Bilateral extraction of maxillary molars yielded 80 specimens, with assessments carried out at two predefined time intervals. To ensure the statistical validity of the experiment, any specimen loss resulting from unexpected technical or histological processing errors was addressed through replacement, thereby maintaining the intended sample size.

2.2. Group assignment and animal preparation

Forty male albino rats aged 8–10 weeks (200–250 grams) with regular dentition were acquired from the animal house of Pharos University, Egypt. Two weeks before teeth extraction, the rats were selected and inspected for exclusion of any general or dental diseases or any prior experimental study[20] The animals received water and food throughout the experimental period and were housed in an environment with controlled temperature and lighting.[21,22]

To minimize potential confounding, accurate random allocation was implemented, whereby treatment status was determined using a computer-generated sequence of random numbers. The participants and all personnel involved in the study were unaware of their treatment assignment.

2.3. Induction of diabetes mellitus (DM)

Before the induction of diabetes, all experimental rats underwent a 12 h fasting period to standardize their baseline metabolic conditions. Diabetes mellitus (DM) was subsequently induced *via* a single intraperitoneal injection of streptozotocin (STZ) at a dose of 50 mg kg^{-1} body weight, freshly dissolved in 0.1 M citrate buffer with a pH of 4.5, just before administration (Sigma-Aldrich, USA). Three days post-injection, fasting blood glucose levels were evaluated *via* a digital glucometer (i-SENS, Inc., South Korea) to verify the onset of diabetes. Rats presenting fasting glucose levels above 250 mg dL^{-1} were regarded as diabetic, by previously established criteria.[23] Blood glucose monitoring was performed regularly during the experimental period to maintain diabetic status.

Open Access Article. Published on 04 February 2026. Downloaded on 2/26/2026 3:16:51 PM.
This article is licensed under a Creative Commons Attribution-NonCommercial 3.0 Unported Licence.

2.4. Tooth extraction procedures

To prevent postoperative infections, all animals received oral antibiotic prophylaxis consisting of spiramycin (7 mg kg^{-1}; Pharaonia Pharmaceuticals, Egypt) and metronidazole (12 mg kg^{-1}; Sanofi Aventis, Egypt), administered three days before tooth extraction. On the day of surgery, diabetic rats were subjected to a short fasting period of 1–2 h. At the same time, unrestricted access to water was maintained to reduce procedural stress and mitigate the risk of hypoglycemia associated with anesthesia.

Bilateral extraction of the mandibular first molars was implemented under general anesthesia.

Firstly, animals received an intramuscular injection of atropine sulfate at a dose of 0.4 mL kg^{-1} to reduce salivary secretions. General anesthesia was then induced using a combination of xylazine 2% (Adwia, 10th of Ramadan City, Egypt) and ketamine hydrochloride 10% (Ketamine Alfasan 10%, Woerden, The Netherlands) at doses of 0.2 mL kg^{-1} and 0.5 mL kg^{-1} body weight, respectively, administered intramuscularly.[24–26]

According to Moghadam *et al.*'s findings, animals belonging to all groups experienced bilateral extraction of their first molar teeth in the mandible.[25] First, an iodine swab was applied to the surgical site. Then, each tooth was luxated using surgical elevators by tipping it slowly in the buccal direction and then in the lingual direction for 1 second in each direction. This was repeated 10 times until the tooth was loosened. After this step, the tooth was easily extracted with the lower remaining root extraction forceps.

After tooth extraction procedures, a total of 40 rats were categorized randomly into four groups ($n = 10$ rats per group).

2.4.1. In Group I (DM). The tooth sockets of diabetic rats were left without any material applied.

2.4.2. In Group II (CS). The tooth sockets of diabetic rats were loaded with CS.

2.4.3. In Group III (Nano-FA). The tooth sockets of diabetic rats were loaded with Nano-FA.

2.4.4. In Group IV (CS–Nano-FA–HPMC). The tooth sockets of diabetic rats were loaded with CS–Nano-FA–HPMC paste.

After placing the experimental materials into the extraction sockets of groups II, III, and IV, the sites were closed using 4–0 black silk sutures to ensure proper wound approximation.[27] Postoperatively, all animal groups received intramuscular administration of Cataflam (Novartis, Egypt) every eight hours for two days to provide analgesia. Additionally, ampicillin was administered at a dose of 25 mg kg^{-1} body weight every eight hours for five days to prevent infection. Rats were monitored daily during the first week for any signs of inflammation, disease, or other postoperative complications.

2.5. Materials used

Chitosan, characterized by a high molecular weight ranging from 600 000 to 800 000 g mol^{-1} (CAS: 9012-76-4), with 75% to 85% degrees of deacetylation, a pH level between 6.5 and 8.0, and a viscosity of 200 to 800 cP; hydroxypropyl methylcellulose (HPMC, molecular weight of 4237 Da, CAS: 9004-65-3; the average viscosity of 1% HPMC in 1% KCl at 25 °C under 60 rpm is nine cP, hydroxypropoxyl group percentage: 30.3%, and methoxyl group percentage: 19.6%), and calcium nitrate tetrahydrate ($Ca(NO_3)_2 \cdot 4H_2O$, formula weight of 236.15 g mol^{-1}, and assay of ≥99.0%), were sourced from Sigma Aldrich, USA. Ammonium fluoride (NH_4F, formula weight of 37.04 g mol^{-1}, and assay >99%), sodium hydroxide (NaOH, formula weight of 40.0 g mol^{-1}, and assay >99%), and diammonium hydrogen phosphate ($(NH_4)_2HPO_4$, formula weight of 132.06 g mol^{-1}, and assay >99%) and were supplied by Merck Company in Germany. Glacial acetic acid (CH_3COOH, formula weight of 60.05 g mol^{-1}, and assay ≥99%), methanol (CH_3OH, formula weight of 32.04 g mol^{-1}, and assay 99.8%), and potassium chloride (KCl, formula weight of 74.55 g mol^{-1} and assay 99.5%) were provided by BDH in the UK.

2.6. Instrumentation for characterization

Throughout this investigation, several characterization procedures were implemented to analyze the structural attributes of the synthesized CS hydrogel, Nano-FA, and the CS–Nano-FA–HPMC nanocomposite hydrogel samples. For intense, Fourier-transform infrared (FT-IR) spectra were recorded with a Bruker Vertex 70 spectrophotometer over the range 450–4500 cm^{-1}. X-ray diffraction (XRD) analysis was conducted using a Shimadzu Lab X 6100 diffractometer (Kyoto, Japan) operating at 40 kV and 30 mA with Cu-Kα radiation ($\lambda = 1.54$ Å), scanning 2θ angles from 10° to 80° with a step size of 0.02° and a counting time of 0.6 s per step at room temperature (25 °C). Morphological and microstructural analyses were carried out using a JEOL JSM-IT200 scanning electron microscope (SEM) equipped with a JEOL-JFC-1100E sputter coater, and a JEOL JSM-1400 Plus high-resolution transmission electron microscope (HR-TEM). Energy dispersive X-ray (EDX) spectroscopy was performed on the JSM-IT200 SEM with an acceleration voltage of 20 kV, working distance of 10 mm, and under high vacuum conditions.

2.7. Synthesis of FA nano-powder

Nano-fluorapatite (Nano-FA) was synthesized using a co-precipitation method adapted from a previous study.[14] A solution of $Ca(NO_3)_2 \cdot 4H_2O$ was stirred for 30 min to ensure complete dissolution. Separately, $(NH_4)_2HPO_4$ was dissolved in double-distilled water and stirred for an equal period, followed by the addition of NH_4F with continued stirring for 30 min. The phosphate-fluoride solution was then added dropwise to the $Ca(NO_3)_2 \cdot 4H_2O$ solution under continuous ammonia addition, with the pH continuously monitored using a calibrated pH meter and maintained above 10 by the gradual addition of aqueous ammonia solution. The reaction was carried out at about 70 °C with continuous stirring at ~500 rpm to promote uniform mixing and reproducibility. The resulting precipitate was collected by centrifugation, dried at 70 °C for 24 h, finely ground into a powder, and stored under controlled conditions for future use.

2.8. Synthesis of CS hydrogel

Chitosan (CS) hydrogel was prepared according to the procedure described by Lu *et al.*[27] detailed, with some modifications

 © 2026 The Author(s). Published by the Royal Society of Chemistry

Open Access Article. Published on 04 February 2026. Downloaded on 2/26/2026 3:16:51 PM.
This article is licensed under a Creative Commons Attribution-NonCommercial 3.0 Unported Licence.

applied. Firstly, 300 mL of 10% (w/v) acetic acid was mixed with 200 mL of methanol to form a homogeneous solution, and the pH was adjusted to 4 using 0.1 M NaOH. CS powder (15 g, 2%) was then gradually introduced to the mixture at a rate of 0.1 mg every 2 min under continuous stirring for 6 h to ensure complete dissolution. Subsequently, a solution of 450 mL ethyl acetate and 450 mL ethanol was added systematically, and the resulting mixture was filtered to separate the solid hydrogel-like material. The solid was washed multiple times using a blend of 90 mL anhydrous ethanol and 2–10 mL ethyl acetate for 30 min, followed by a second filtration. Double-distilled water was then added to the filtered material, which was transferred into a rotary evaporation flask and concentrated at 60 °C. The concentrated hydrogel was finally freeze-dried for 48 h to obtain a fine, stable powder appropriate for further characterization.

2.9. Synthesis of CS–Nano-FA–HPMC nanocomposite hydrogel

The assembly of the CS–Nano-FA–HPMC nanocomposite hydrogel involved mixing the prepared CS hydrogel, the synthesized Nano-FA powder, and hydroxypropyl methylcellulose (HPMC) in a mass ratio of 1 : 1 : 3.[28,29] Following the ratio above, the adequate amounts of Nano-FA were gradually introduced into the appropriate proportions of the CS hydrogel solution. The resulting mixture was subsequently subjected to ultrasonic stirring for 15 min, followed by magnetic stirring for 90 min at 45 °C to ensure the uniformity and effective dispersion of the Nano-FA throughout the CS hydrogel polymer matrix. Afterward, HPMC powder at a concentration of 2% (w/v) was dissolved in distilled water within a separate beaker, and 75% of the original volume evaporated. The solution is permitted to reach room temperature. Subsequently, the viscous solution was progressively added to the CS–Nano-FA–HPMC hydrogel at room temperature and stirred until a consistent white suspension was formed. It is worth mentioning that, in this method, HPMC acted as both a thickening agent and a cross-linking agent when incorporated into the nanocomposite.[30] The resulting CS–Nano-FA–HPMC nanocomposite hydrogel was then placed into a scaffold mold and underwent the freeze-thaw process, which involved freezing the mixture at −20 °C for 18 h and thawing at 25 °C for 6 h. Finally, the scaffold was removed from the mold and characterized using XRD, EDX, SEM, and FTIR to verify the successful formation and structural integrity of the nanocomposite hydrogel. A schematic illustration depicting the synthesis steps of Nano-FA, the preparation of CS hydrogel, and the fabrication process of the CS–Nano-FA–HPMC nanocomposite hydrogel scaffold is presented in Scheme 1.

2.10. Animal euthanization

After extracting the mandibular first molar, five rats in each group were euthanized at the 2 week and 6 week marks, respectively.

2.11. Biochemical analysis

Upon completion of each follow-up period, the animals were anesthetized, and blood samples were collected *via* sterile cardiac puncture. The collected blood was allowed to clot at room temperature for 20–30 min, after which the serum was separated by centrifugation at 3000 rpm for 10–15 minutes at 4 °C. The resulting serum was carefully transferred into sterile Eppendorf tubes and either immediately subjected to analysis or stored at −80 °C to maintain protein stability and prevent degradation from repeated freeze–thaw cycles. Portions of the collected serum samples were immediately used to evaluate specific biochemical markers. The levels of TNF-α (Elabscience, Catalog No. E-EL-R2856), IL-1β (Thermo Fisher Scientific, Catalog No. BMS630ALP), TGF-β1 (Elabscience, Catalog No. E-EL-0162), and osteocalcin (Thermo Fisher Scientific, Catalog No. EEL123) were measured *via* enzyme-linked immunosorbent assay (ELISA) tools following the procedures specified by the manufacturers.

In addition, the activity of alkaline phosphatase (ALP) was determined using a colorimetric assay (Sigma-Aldrich, USA).[31,32]

2.12. Histological evaluation

Following mandibular dissection, the left half of each mandible was prepared for light microscopy (LM) evaluations to examine the histological variations in tissue structure across the groups. Following the established procedure, samples were decalcified, fixed in 10% formalin, and embedded in paraffin blocks. After sectioning the samples (5 μm sections), they were stained with Masson trichrome, hematoxylin, and eosin (H&E). Histological analysis by two investigators was performed using LM with a digital camera (Leica ICC50 HD), and pictures of characteristic areas were taken and labelled.[33]

2.13. LM histomorphometric analysis

The H&E-stained sections were analyzed morphometrically to determine the percentage of new bone development across the four groups.[34] The newly formed bone was identified based on standard morphological criteria, including the presence of numerous prominent osteocytes within their lacunae, an irregular collagen matrix, and evidence of mineralization.[35,36] Images were evaluated using ImageJ software (National Institutes of Health, USA).

2.14. Scanning electron microscopy (SEM) evaluation

An SEM Model Quanta 250 FEG (Field Emission Gun) was used to examine the bone surfaces in each group's socket area of the right side of the jaws, after the soft tissues had been thoroughly removed. The JFC-1100E-IEOL ion sputtering evaporator was then used to properly dry and gold-plate the samples. An SEM (JEOL-JSM-5200LV, Tokyo, Japan) was then used to correct them.[37]

2.15. Statistical analysis

After entering the LM histomorphometric and EDX analysis data into the computer, the analysis was conducted using IBM

Open Access Article. Published on 04 February 2026. Downloaded on 2/26/2026 3:16:51 PM.
This article is licensed under a Creative Commons Attribution-NonCommercial 3.0 Unported Licence.

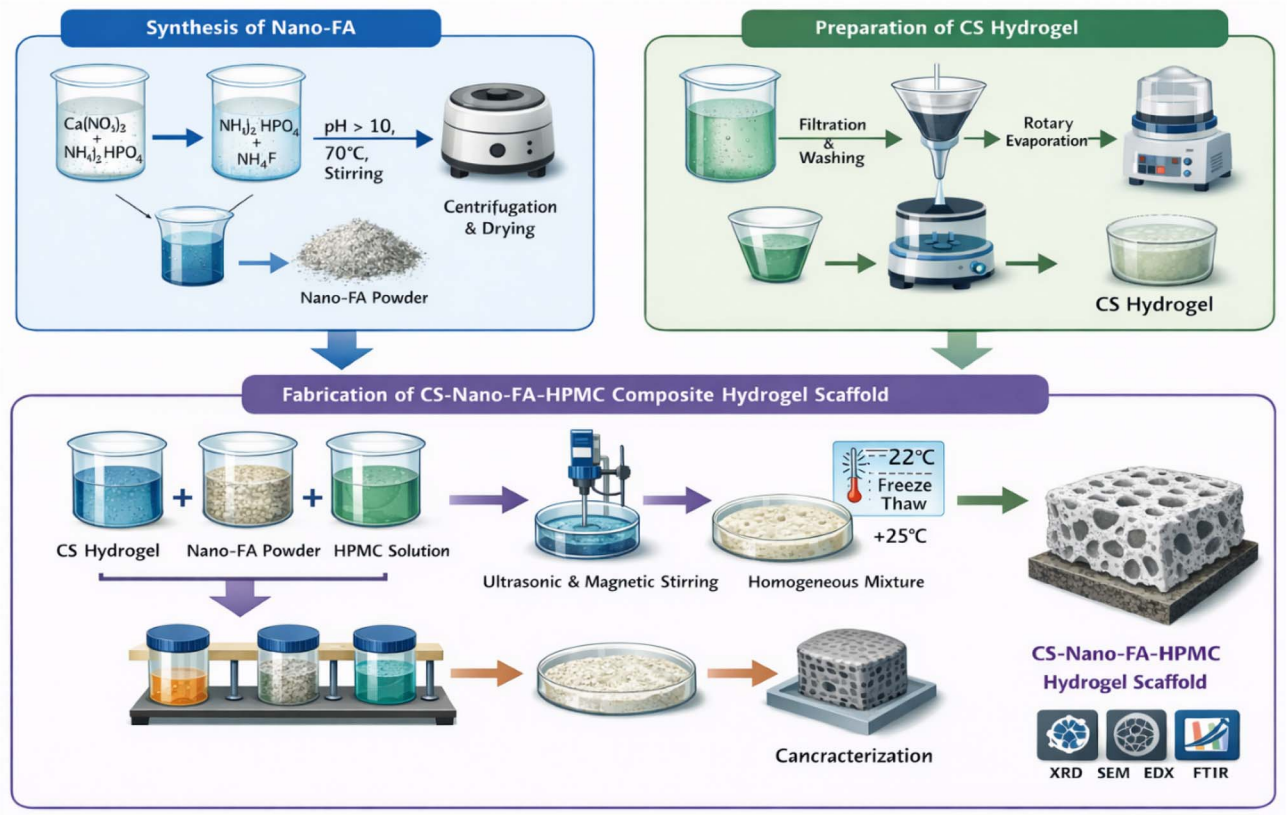

Scheme 1 Schematic illustration of the main preparation steps, including the synthesis of nano-fluorapatite (Nano-FA), the formation of the chitosan (CS) hydrogel, and the fabrication of the CS–Nano-FA–HPMC nanocomposite hydrogel scaffold.

SPSS version 20.0 (Armonk, NY: IBM Corp.). After an ANOVA, a *post hoc* test (Tukey) was applied to evaluate the overall differences between the control and the other three groups. At the 5% level, the significance of all collected results was assessed. The chance of the three experimental groups' disparate outcomes will be predicted by statistical probability.[38]

3. Results

3.1. Clinical observations

Throughout the experimental period, the overall behavior of diabetic rats in all four groups was monitored. The animals remained active, exhibited no distress, and maintained normal feeding behaviors. Although diabetes is typically associated with weight loss, no significant alterations in body weight were observed among the groups during the study. Every treatment group of animals recovered without major issues and was euthanized on time. During the trial, no rats dropped out.

3.2. Characterization of the CS–Nano-FA–HPMC nanocomposite hydrogel

3.2.1. FT-IR spectroscopy. The primary step in establishing the effectiveness of the synthesis process is the FT-IR. This technique is regarded as an excellent method for validating the incorporation process among the components of the as-synthesized nanocomposite hydrogel. Fig. 1 displays the FT-IR spectra corresponding to CS, Nano-FA, HPMC, and the CS–Nano-FA–HPMC nanocomposite hydrogel. The FT-IR spectrum of CS is illustrated in Fig. 1a, distinctly displaying a broad band at 3483.14 cm^{-1}, which indicates the stretching vibrations of –OH and N–H groups along with their associated hydrogen bonds[39] A peak located at 1412.13 cm^{-1} corresponds to the symmetrical deformation mode of $-CH_3$.[39] The weak peak identified at 1345.82 cm^{-1} primarily arises from the stretching frequency of the O=C–O group. Meanwhile, the additional two weak peaks recorded at 1222.65 and 1023.51 cm^{-1} can be understood as the asymmetric stretching vibration mode of the C–O–C etheric bridge and the deformations of the C–O group, respectively.[40] The weakly defined peaks for amide I and amide II were detected at 1644.42 and 1559.03 cm^{-1}, respectively, which corroborates the considerable level of deacetylation of CS.[40] The observed peak at 1559.03 cm^{-1} can also be related to the C=N formed Schiff base, thereby supporting the cross-linking agent's identification and confirming the successful cross-linking and enhancing.[1,2] Furthermore, the band located at 923.97 cm^{-1} is ascribed to the synergistic effects of the C–N stretching vibration associated with primary amines and the C–O stretching vibration originating from the primary alcohol in CS hydrogel.[41] A band at 680 cm^{-1}, indicative of an angular distortion about H–N–H bonds, was also identified.[28]

Fig. 1b represents the synthesized Nano-FA spectrum, which shows a variety of distinct peaks. As indicated in previous

 © 2026 The Author(s). Published by the Royal Society of Chemistry

Open Access Article. Published on 04 February 2026. Downloaded on 2/26/2026 3:16:51 PM.
This article is licensed under a Creative Commons Attribution-NonCommercial 3.0 Unported Licence.

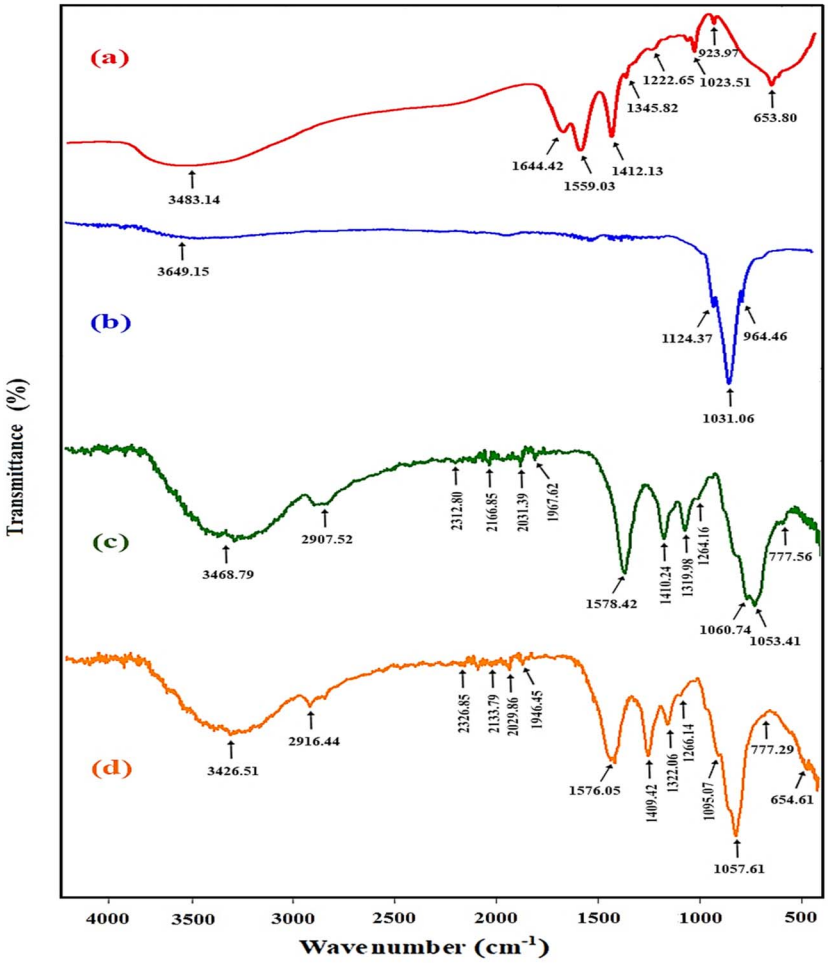

Fig. 1 FT-IR spectra of (a) CS hydrogel, (b) Nano-FA, (c) HPMC, and (d) the CS–Nano-FA–HPMC nanocomposite hydrogel.

investigations, the weak band located at 3649.15 cm^{-1} is associated with the OH–F band.[42] Accordingly, the detection of this peak suggests the formation of fluoride-substituted hydroxyapatite (HA). The vibrations within the 1400–900 cm^{-1} range, related to the stretching modes of PO_4, were characterized as the unique peaks of pure apatite, confirming the complete formation of apatite[43] A significant band of PO_4 was detected at 1031.06 cm^{-1}. Additionally, the prominent bands observed at 1124.37 and 964.46 cm^{-1} correspond to the ν_1 and ν_2 vibrational modes of the phosphate (PO_4) group, respectively.[43]

The FT-IR spectrum of HPMC (Fig. 1c) exhibits several notable absorption bands, indicating the functional groups and structural attributes of this material. The significant broad band observed at 3468.79 cm^{-1} indicates the stretching vibrations of the –OH groups in the HPMC molecule.[44] On the other hand, the weak band corresponding to the bending vibrations of the C–O–H bonds in hydroxyl groups is observable at 1319.98 cm^{-1}. The additional significant peak, typically at about 1053.41 cm^{-1}, indicates the glucose ring found in HPMC, whereas the absorption band at 1578.24 cm^{-1} results from C=C stretching vibrations.[45] For the C–O and C–H stretching vibrations, respectively, absorption bands at 1060.74 and 2907.32 cm^{-1} were noted.[46] The peaks identified at 2312.80, 2166.85, 2031.39, and 1978.42 cm^{-1} designate the C=O stretching vibration of the six-membered ring within the molecular structure of HPMC.[44] Additionally, the distinctive peaks related to the methoxy ($-OCH_3$) group, the vibration of the C–O–C pyranose ring, and the band linked to the β-glycosidic bond were observed at 1410.24, 1264.16, and 777.58 cm^{-1}, respectively.[44,45]

The FT-IR spectrum of CS–Nano-FA–HPMC is depicted in Fig. 1d, clearly showing several significant peaks associated with the functional groups of the nanocomposite components, along with a slight shift in wavenumber and variations in peak intensity. In comparison to the CS hydrogel spectrum (Fig. 1a), it is evident that the spectrum of CS–Nano-FA–HPMC displays new peaks that correspond to Nano-FA (Fig. 1b), along with the distinctive peaks of HPMC (Fig. 1c). The absorption bands found at 1057.61 and 2029.86 cm^{-1} are linked to C–O and C–H groups. In contrast, the peaks at 2326.85, 2133.79, 2029.86, and 1946.45 cm^{-1} are assigned to the C=O stretching vibration of the six-membered ring of HPMC.[44] Furthermore, the peaks observed at 3483.14, 1644.42, and 1559.03 cm^{-1} displayed the distinctive overlapping peak between the components of HPMC and CS. These peaks are shifted towards lower wave numbers, suggesting a reduction in free O–H/N–H stretching, ascribed to

Open Access Article. Published on 04 February 2026. Downloaded on 2/26/2026 3:16:51 PM.
This article is licensed under a Creative Commons Attribution-NonCommercial 3.0 Unported Licence.

the formation of stronger intermolecular hydrogen bonds among the CS, Nano-FA, and HPMC molecules. Shahzad *et al.* also reported the infrared-shifted peak corresponding to O–H stretching in their study on synthesizing carboxymethyl/CS/gelatin/PEG–GO nanocomposite hydrogel.[40] Identifying the vibrational modes of CS, Nano-FA, and HPMC in the spectra of CS–Nano-FA–HPMC signifies the successful synthesis of this nanocomposite hydrogel.

3.2.2. X-ray diffraction (XRD). Using X-ray diffraction techniques, the structural properties of CS hydrogel, Nano-FA, and the as-synthesized CS–Nano-FA–HPMC nanocomposite hydrogel were investigated, with the results depicted in Fig. 2. The X-ray diffraction (XRD) pattern of the freeze-dried CS hydrogel powder (Fig. 2a) reveals the coexistence of amorphous and crystalline phases, indicated by a prominent peak at $2\theta = 22.31°$, a less intense peak at $2\theta = 10.86°$, and an additional diffraction peak observed near $2\theta = 26.45°$.[47] These diffraction peaks align with the semi-crystalline characteristics of CS and are corroborated by the JCPDS file no. 039-1894.[48] The first two peaks are associated with hydrated and anhydrous crystalline structures, whereas a broadened, distinctive peak signifies the presence of the amorphous region.[28] Fig. 2b displays the XRD pattern of the prepared Nano-FA. The peak lines that represent the FA phase are distinctly observable in the figure. The X-ray diffractogram of the tested sample validated that the nano-crystalline fluorapatite $Ca_5(PO_4)_3F$ is present in a pure crystal phase. All diffraction peaks obtained for FA are consistent with the standard pattern of fluorapatite (JCPDS file no. 15-0876), characterized by a hexagonal structure.[48] Additionally, Fig. 2b clearly shows that the XRD patterns of Nano-FA exhibit no detectable impurity peaks or secondary crystalline phases.

The pristine CS and Nano-FA diffractograms were used as reference standards to interpret the X-ray patterns observed for the CS–Nano-FA–HPMC nanocomposite hydrogel (Fig. 2c). Notably, the X-ray diffractogram of the nanocomposite exhibited peak broadening, indicating a significant rise in the amorphous phase at the expense of the crystalline phase compared to that of pure CS (Fig. 2a). The absence of the CS-specific peak at $2\theta = 10.86°$ along with a significant decrease in the intensities of the peaks at 22.31° and 26.45° further validated this observation. The observed reduction in crystallinity of the CS–Nano-FA–HPMC nanocomposite hydrogel was attributed to the intermolecular interactions between HPMC and CS, as well as the excellent miscibility of the two polymers in the blended hydrogel, which limited the rearrangement of HPMC's molecular chains.[49] A similar finding was noted regarding the HPMC-CMC film, with a decrease in the HPMC crystalline plane.[50] Furthermore, Fig. 2c clearly illustrates a slight shift in the peak associated with CS, suggesting a potential cross-linking between HPMC and CS.[10] The patterns further revealed new distinctive peaks of Nano-FA, which appeared at their expected positions and were consistent with the corresponding quantities in the nanocomposite hydrogel. Nonetheless, Nano-FA content did not influence the crystallinity level of the CS–Nano-FA–HPMC nanocomposite hydrogel.[51] These findings

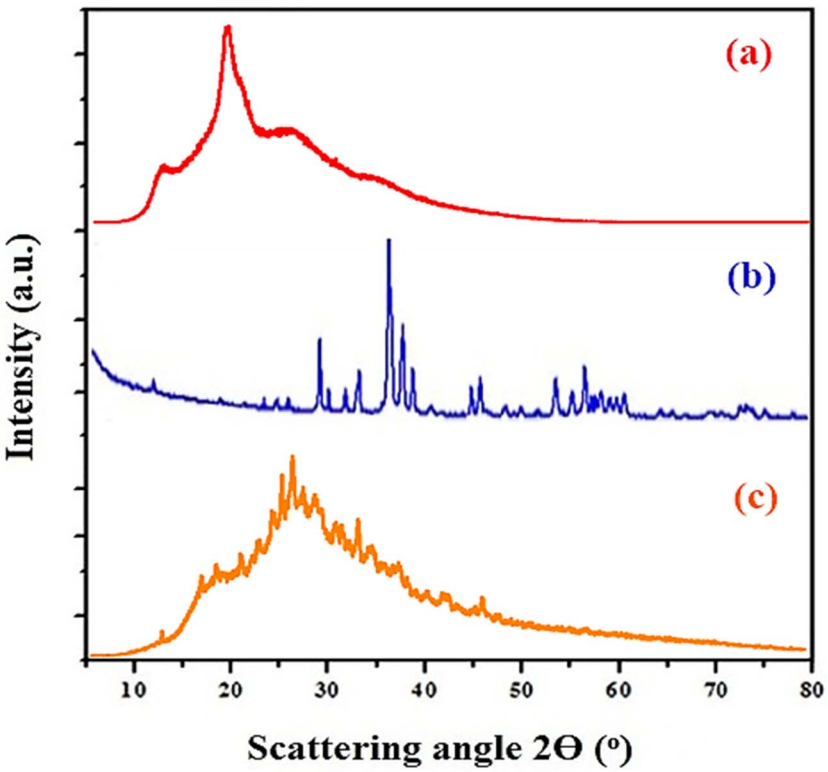

Fig. 2 XRD patterns of (a) CS hydrogel, (b) Nano-FA, and (c) the CS–Nano-FA–HPMC nanocomposite hydrogel.

 © 2026 The Author(s). Published by the Royal Society of Chemistry

Open Access Article. Published on 04 February 2026. Downloaded on 2/26/2026 3:16:51 PM.
This article is licensed under a Creative Commons Attribution-NonCommercial 3.0 Unported Licence.

robustly indicate that CS–Nano-FA–HPMC synthesis was effectively achieved under the specified conditions.

3.2.3. Microstructural analysis using SEM and TEM. To fully grasp the properties of hydrogels and their porous structure, the effectiveness of the freeze-dried CS–Nano-FA–HPMC nanocomposite hydrogel in biological applications is largely dependent on its morphology and particle size, which are mainly analyzed through microstructural characterization methods, including SEM and TEM, in this work. A pristine CS hydrogel was prepared for comparative morphological studies without including Nano-FA or HPMC. The SEM image depicting the synthesized Nano-FA (Fig. 3a) exhibits semi-spherical and hexagonal structures, with a particle size measuring 25.36 nm. The HR-TEM image (Fig. 3b) presents similar findings, validating that Nano-FA particles displayed a typical needle-like shape with minor variations in particle size as observed in the SEM image. Furthermore, the Nano-FA particles were noted to be non-agglomerated and evenly distributed.

Alternatively, the SEM images of the CS hydrogel (Fig. 3c) and the CS–Nano-FA–HPMC nanocomposite hydrogel (Fig. 3d) display a rough, interconnected, and complex three-dimensional network structure. This structure is characterized by longitudinal tubes featuring microchannels that present an irregular pattern, a typical characteristic of CS-based gels.[45] Incorporating HPMC increases surface roughness, decreases pore size, enhances network density, and maintains phase continuity within the gel matrix. Consequently, the resulting nanocomposite hydrogel exhibits a more homogeneous and denser microstructure, as depicted in Fig. 3d. This phenomenon may arise from intermolecular hydrogen bonding between CS and HPMC.[52] The gel matrix consistently observed in Fig. 3d results from the development of triple-helix cores, which subsequently undergo growth, leading to the formation of pores due to ice crystal sublimation during the freeze-drying process.[45,52] Additionally, the surface morphology of the CS–Nano-FA–HPMC nanocomposite hydrogel (Fig. 3d) revealed that Nano-FA is present as white particles incorporated within the hydrogel framework, characterized by a consistent dispersion alongside slight agglomeration. Nonetheless, the hydrogen bonds formed at the molecular level contribute to a denser arrangement between Nano-FA and the CS/HPMC matrix, which consequently minimizes the occurrence of agglomerations in the resulting nanocomposite hydrogel. Moreover, the SEM images of the CS–Nano-FA–HPMC nanocomposite hydrogel did not reveal any isolated or phase-separated components, suggesting that Nano-FA, CS, and HPMC were entirely compatible. The findings from SEM and TEM can be directly utilized to

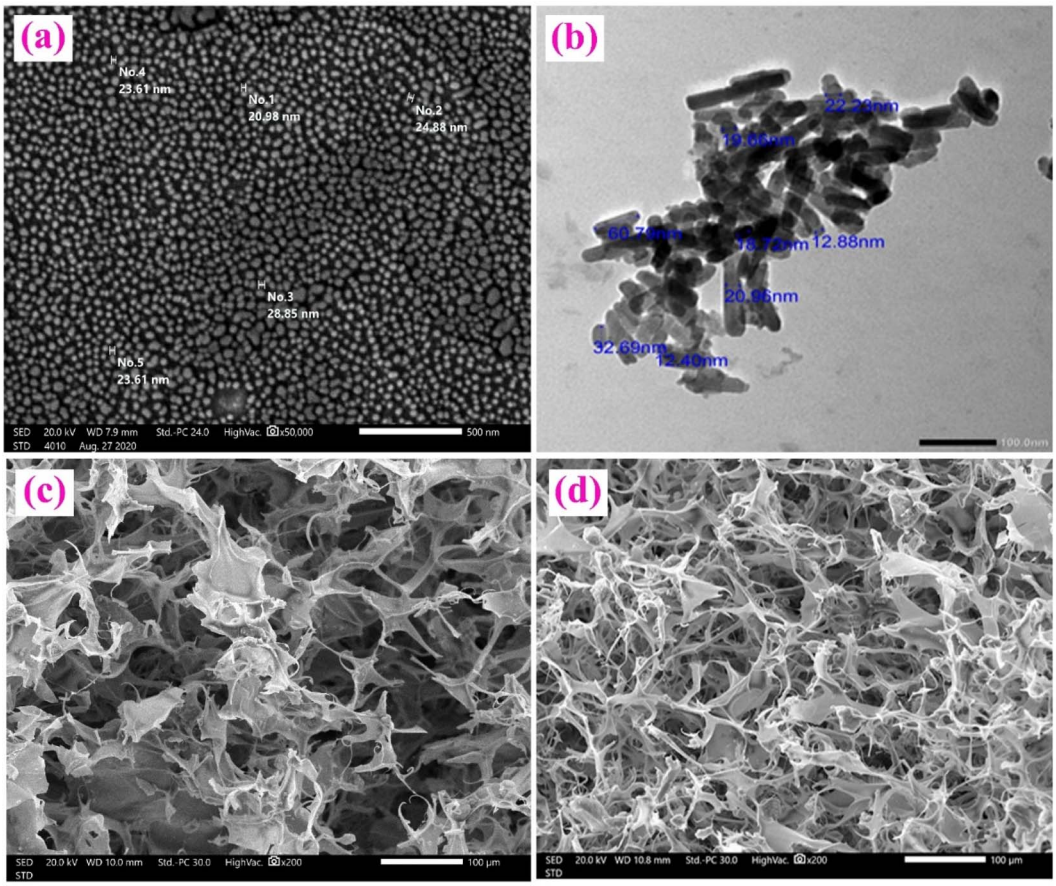

Fig. 3 (a) SEM image of Nano-FA. (b) TEM image of Nano-FA. (c) SEM image of the CS hydrogel, (d) SEM image of the CS–Nano-FA–HPMC nanocomposite hydrogel.

Open Access Article. Published on 04 February 2026. Downloaded on 2/26/2026 3:16:51 PM.
This article is licensed under a Creative Commons Attribution-NonCommercial 3.0 Unported Licence.

explain the successful preparation and formation of the CS–Nano-FA–HPMC nanocomposite hydrogel.

3.2.4. Energy dispersive X-rays (EDX). EDX analysis was employed to determine the elemental composition of Nano-FA and the newly designed CS–Nano-FA–HPMC nanocomposite hydrogel, as illustrated in Fig. 4. In the EDX spectrum analysis of Nano-FA (Fig. 4a), peaks are observed for O (40.67%), F (10.69%), P (14.07%), and Ca (28.42%), in addition to slight traces of Si and C impurities. These results confirm the practical synthesis of FA nano-powder. The EDX spectrum and elemental analysis of the CS–Nano-FA–HPMC nanocomposite hydrogel, presented in Fig. 4b, indicated that the composition of the sample consisted of 30.89% C, 46.87% O, 2.28% F, 2.68% P, and 7.17% Ca, along with various trace elements. The significant mass percentage of oxygen and carbon elements detected in the EDX spectra of the CS–Nano-FA–HPMC nanocomposite hydrogel can be attributed to the presence of CS and HPMC. The identification of peaks corresponding to P, F, and Ca elements in the EDX spectrum of the CS–Nano-FA–HPMC nanocomposite hydrogel supports the dispersion and physicochemical bonding of Nano-FA in the hydrogel's composite structure, further confirming the successful synthesis of the designed nanocomposite.

3.3. Physicochemical characterization and functional performance of the CS–Nano-FA–HPMC hydrogel

The CS–HPMC–Nano-FA hydrogel demonstrated a viscosity of 20 660 ± 35 cP, confirming an injectable yet structurally stable profile suitable for placement inside the extraction socket. This test was carried out using a Brookfield DV-II + Pro RV rotational viscometer (AMETEK Brookfield, Middleboro, MA, USA) with spindle RV-3 at a rotational speed of 20 rpm. Viscosity and flow behavior were assessed using a Brookfield DV-II + Pro RV rotational viscometer (AMETEK Brookfield, Middleboro, MA, USA) with spindle RV-3 at a rotational speed of 20 rpm. Approximately 25 mL of the formulation was placed, ensuring correct immersion of the spindle. The temperature was maintained at 25 ± 0.5 °C, readings were taken in triplicate and reported in centipoise (cP).

The spreadability test showed a mean spread diameter of approximately 2 cm, indicating moderate spreading behavior that supports positional stability and minimizes early wash-out.

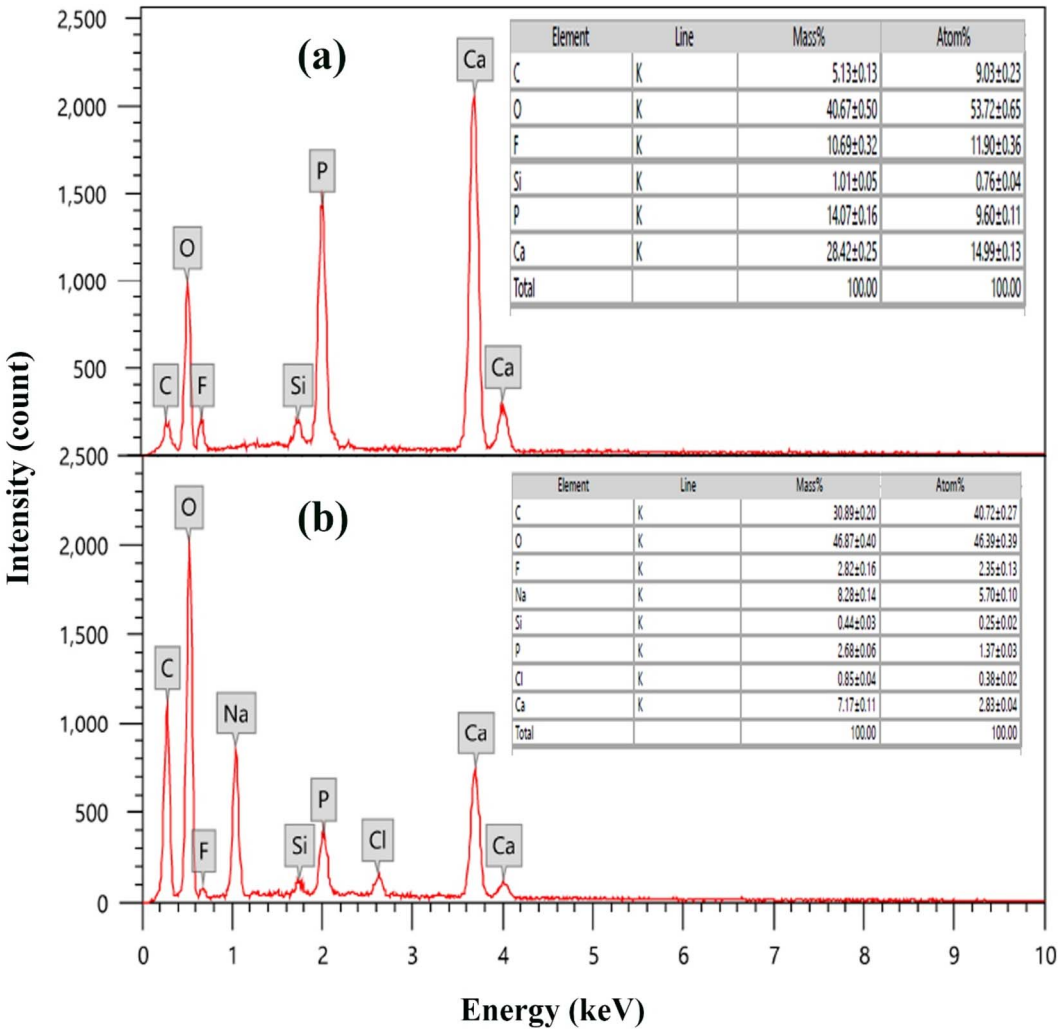

Fig. 4 EDX spectra (a) Nano-FA, (b) The CS–Nano-FA–HPMC nanocomposite hydrogel.

 © 2026 The Author(s). Published by the Royal Society of Chemistry

Open Access Article. Published on 04 February 2026. Downloaded on 2/26/2026 3:16:51 PM.
This article is licensed under a Creative Commons Attribution-NonCommercial 3.0 Unported Licence.

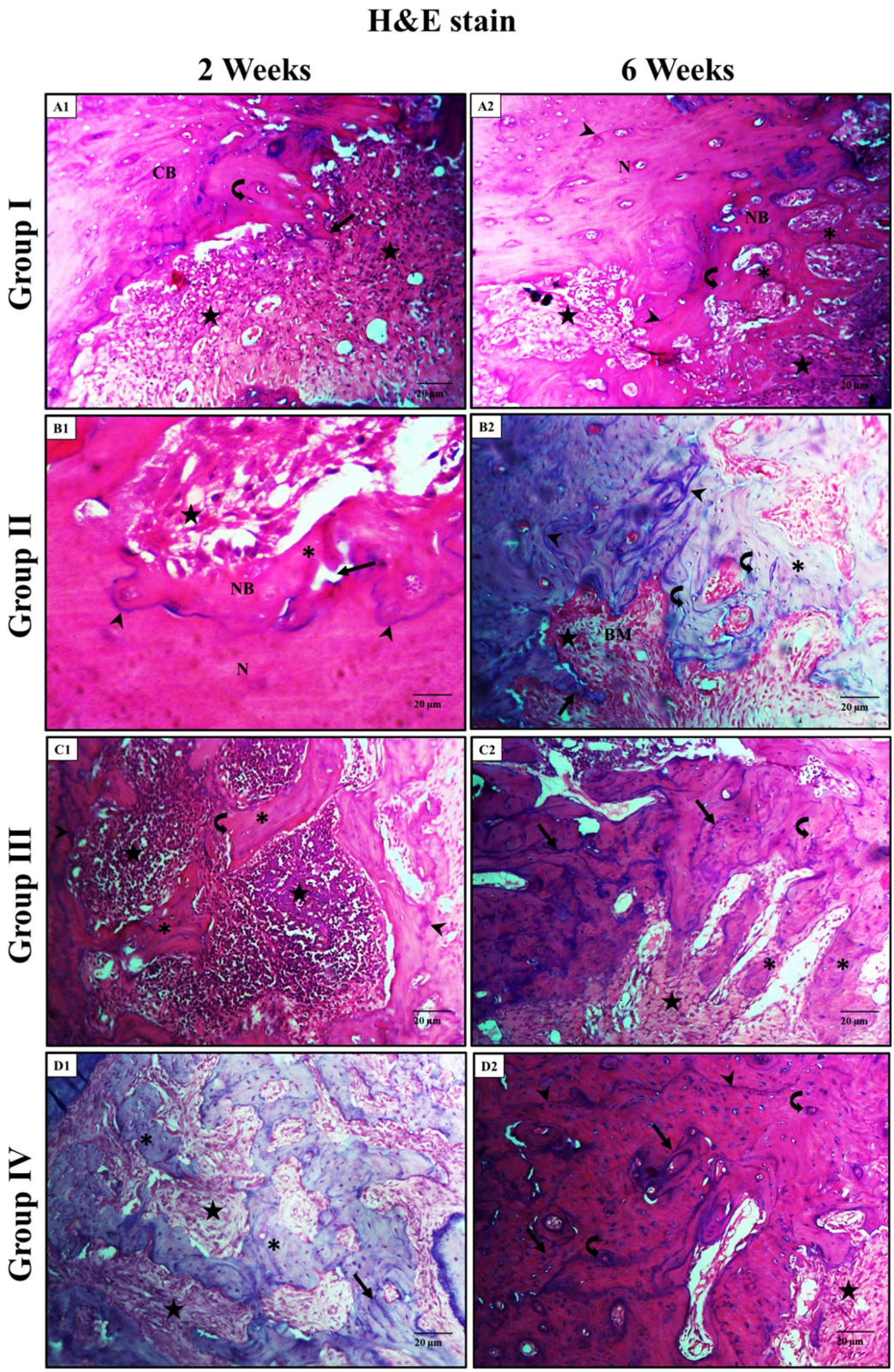

Fig. 5 Light micrographs of H and E stain for the socket area in all groups. (A1 and A2) Group I (DM) at 2 and 6 weeks, show nearly no bone formed inside the socket as it is filled with granulation tissue (star). Note the thin bone trabecula (arrow) from the socket wall (CB) with osteocytes (curved arrow) inside. At 6 weeks, there is an increase in the bone inside the socket in the form of thin bone trabeculae with less granulation tissue (star), more osteocytes (curved arrow), and more bone resting lines (arrowheads) than in week 2. (B1 and B2) Group II (CSNPs) at 2 and 6 weeks, showing bone resting lines (arrowheads) demarcating the fusion between the new (NB) and native (N) bones except at a space between them (arrow). Also, the granulation tissue (star) is easily detected in larger amounts at week 2 than at week 6. In week 6, the mature bone fills most of the socket area, with thin bone trabeculae (*) radiating from the socket walls. (C1 and C2) Group III (Nano-FA) at 2 and 6 weeks, respectively,

Open Access Article. Published on 04 February 2026. Downloaded on 2/26/2026 3:16:51 PM.
This article is licensed under a Creative Commons Attribution-NonCommercial 3.0 Unported Licence.

During this test, 0.5 g of gel was placed in a circle of 1 cm diameter on a 20 × 20 cm glass plate, a weigh of 500 g was placed over the second glass and allowed to rest for 5 min, the increase in the diameter of gel due to spreading was recorded.

The extrudability assessment revealed a force requirement of 40 g cm^{-2} to initiate continuous flow from a syringe, reflecting moderate resistance to extrusion and appropriate clinical deliverability without excessive manual pressure ($n = 3$, mean ± SD). In this test, CS–HPMC–Nano-FA was filled into a 40 mL disposable syringe without a needle, ensuring elimination of air bubbles. The syringe was positioned vertically, and incremental weights were applied to the plunger until steady extrusion was initiated. The minimal mass required to sustain continuous flow was recorded, and extrudability was calculated as (g cm^{-2}). The extrudability of the formulation was calculated according to the following equation:[54]

$$\text{Extrudability} = \frac{W}{A} \tag{1}$$

where W is the weight applied (g) to extrude the gel from de tube and A is the area (cm^2) of the extruded hydrogel from the tube. The data obtained were expressed as the mean ± SD of three replicates.

The rheological, spreadability, and extrudability findings confirmed that the developed hydrogel possessed an injectable yet retention-stable behavior appropriate for socket application, while histological observations demonstrated progressive *in vivo* replacement of residual material by newly formed trabecular bone, indicating gradual scaffold resorption and functional integration.

Furthermore, in the prepared CS–Nano-FA–HPMC hydrogel system, HPMC plays a dual functional role as both a thickening and physical cross-linking agent. The hydroxyl groups of HPMC are capable of forming hydrogen-bond interactions with the amino and hydroxyl groups present in chitosan, which reinforces the polymeric network and enhances the viscosity, cohesiveness, and mechanical stability of the hydrogel matrix. These non-covalent interactions also contribute to improved structural integrity and influence the swelling and viscoelastic behavior of the hydrogel. Similar hydrogen-bond-mediated interactions between chitosan and HPMC have been reported in previous studies,[54,55] where the incorporation of HPMC was shown to strengthen the hydrogel network and modify its physicochemical properties.

3.4. Light microscopic results

3.4.1. H&E stain results

3.4.1.1 Group I (DM). At 2 and 6 weeks, nearly no bone formed inside the socket, and it appeared filled with granulation tissue, with only the thin bone trabeculae from the socket wall and containing osteocytes. At 6 weeks, there is an increase in the bone inside the socket in the form of thin bone trabeculae with less granulation tissue, more osteocytes, and more bone resting lines than in week 2 (Fig. 5 – A1 and A2).

3.4.1.2 Group II (CS). At 2 and 6 weeks, bone resting lines demarcate the fusion between the new and native bones, except at a space between them, where the granulation tissue is easily detected in larger amounts at week 2 than at week 6. In week 6, the mature bone fills most of the socket area, with thin bone trabeculae radiating from the socket walls (Fig. 5 – B1 and B2).

3.4.1.3 Group III (Nano-FA). At 2 and 6 weeks, more osteocytes were entrapped inside the newly formed bone trabeculae radiating from the wall, and the number increased at week 6 than at week 2 around the granulation tissues. More bone remodelling lines are depicted at week 6 (Fig. 5 – C1 and C2).

3.4.1.4 Group IV (CS–Nano-FA–HPMC). At 2 and 6 weeks, there was more trabecular bone formation with less fibrous tissue and bone remodelling lines. In week 6, there was increased bone formation, with more prominent bone remodelling lines and entrapped osteocytes (Fig. 5 – D1 and D2).

3.4.2. Masson trichrome stain results

3.4.2.1 Group I (DM). At 2 and 6 weeks, less bone formed inside the socket around a large amount of granulation tissue, fewer osteocytes inside, and fewer bone resting lines. At 6 weeks, there was an increase in the bone inside the socket with less granulation tissue, more osteocytes, and more bone resting lines than in week 2 (Fig. 6 – A1 and A2).

3.4.2.2 Group II (CS). At 2 and 6 weeks, compared to Group I, more osteocytes were entrapped within the newly formed bone, with a greater number of bone resting lines. Also, the osteons were formed inside the new bone. The granulation tissues were more easily detected in large amounts at week 2 than at week 6 (Fig. 6 – B1 and B2).

3.4.2.3 Group III (Nano-FA). At 2 and 6 weeks, compared to groups I and II, more osteocytes were captured inside the newly formed bone, and more bone remodelling lines and osteon formation were depicted inside the new bone. Additionally, mixed fibrous and granulation areas were more easily detected in large quantities at week 2; however, by week 6, only fibrous tissue could be depicted (Fig. 6 – C1 and C2).

3.4.2.4 Group IV (CS–Nano-FA–HPMC). At 2 and 6 weeks showed more bone formation with less fibrous tissue, more bone remodelling lines, osteon formation, and entrapped osteocytes compared to group III. In week 6, compared to week 2, there was increased bone formation, characterized by more bone remodeling lines, osteon formation, and entrapped osteocytes (Fig. 6 – D1 and D2).

3.4.3. SEM results

3.4.3.1 Group I (DM). At 2 and 6 weeks, a well-defined socket area was surrounded by the socket wall, with a few thin, short

showing more osteocytes (curved arrow) entrapped inside the newly formed bone trabeculae (*) that are radiated from the wall and increased at week 6 than at week 2 around the granulation tissues (star). More bone remodelling lines (arrow) are depicted at week 6. (D1 and D2) Group IV (CSNPs + Nano-FA) at 2 and 6 weeks, respectively, showing more trabecular bone formation (*) with less fibrous tissue (star), bone remodelling lines (arrow). In week 6, there is more bone formation, with increased bone remodelling lines (arrow) and entrapped osteocytes (curved arrow) (H&E stain X 400).

 © 2026 The Author(s). Published by the Royal Society of Chemistry

Open Access Article. Published on 04 February 2026. Downloaded on 2/26/2026 3:16:51 PM.
This article is licensed under a Creative Commons Attribution-NonCommercial 3.0 Unported Licence.

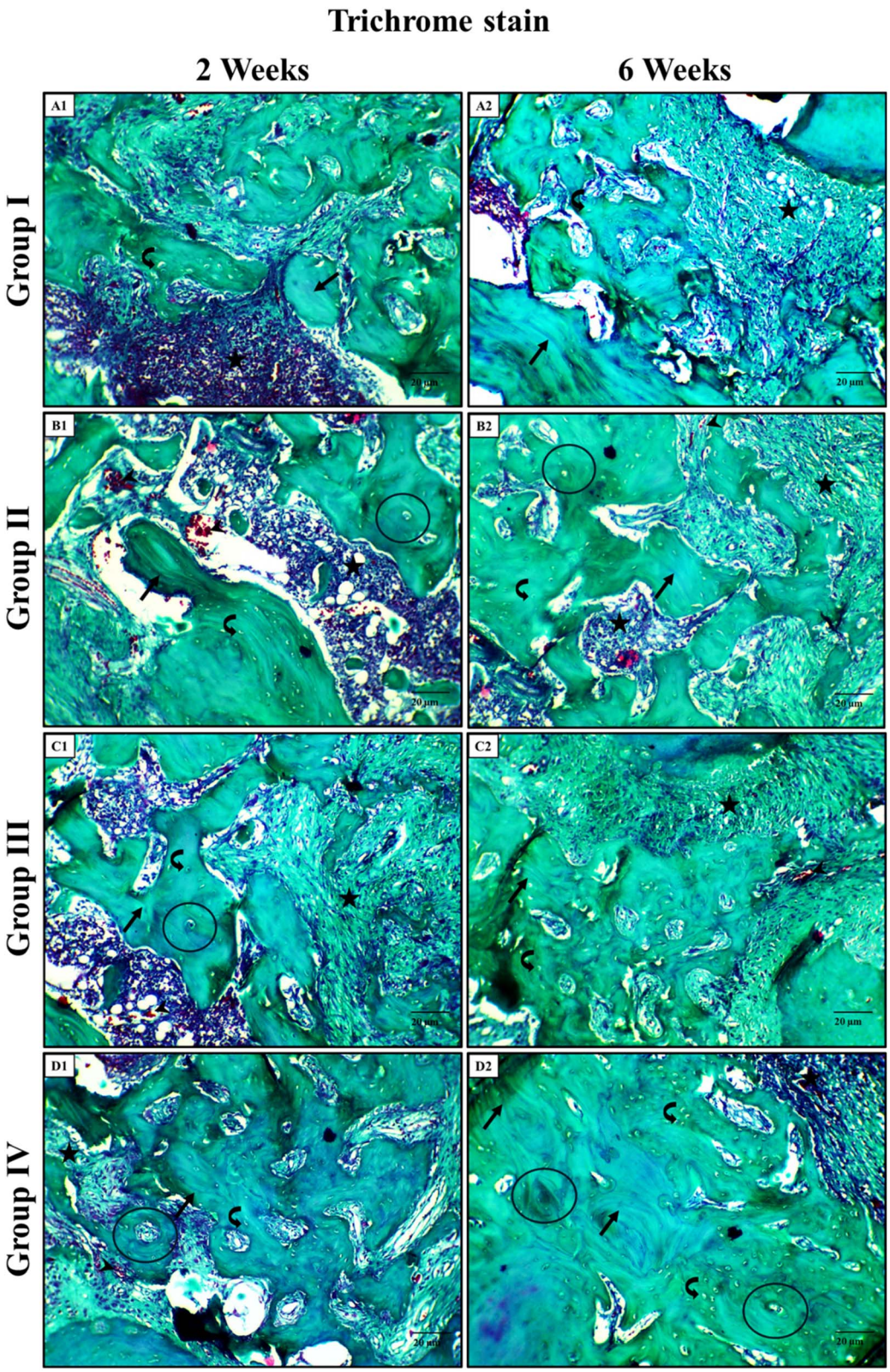

Fig. 6 Light micrographs of Gomori trichrome stain for the socket area in all groups. (A1 and A2) Group I (DM) at 2 and 6 weeks, respectively, showing less bone formed inside the socket with a large amount of granulation tissue (star), fewer osteocytes (curved arrow), and fewer bone resting lines (arrow). At 6 weeks, there is an increase in the bone inside the socket with less granulation tissue (star), more osteocytes (curved arrow), and more bone resting lines (arrow) than in week 2. (B1 and B2) Group II (CSNPs) at 2 and 6 weeks, showing more osteocytes (curved arrow) entrapped inside the newly formed bone, and more bone resting lines (arrow). Note the osteon formation inside the new bone (circled area). Also, the granulation tissue (star) is more easily detected in large amounts at week 2 than at week 6. (C1 and C2) Group III (Nano-FA) at 2 and 6 weeks, respectively, showing more osteocytes (curved arrow) captured inside the newly formed bone, and more bone remodelling lines

Open Access Article. Published on 04 February 2026. Downloaded on 2/26/2026 3:16:51 PM.
This article is licensed under a Creative Commons Attribution-NonCommercial 3.0 Unported Licence.

bone trabeculae arising from the wall. At 6 weeks, the thin, irregular bone trabeculae were increased in number around wide bone marrow spaces (Fig. 7 – A1 and A2).

3.4.3.2 Group II (CS). At 2 and 6 weeks, compared to group I, it revealed a narrow socket area surrounded by the socket wall with thin, short bone trabeculae arising from the wall. At 6 weeks, the thin bone trabeculae were increased in number around the narrow bone marrow spaces (Fig. 7 – B1 and B2).

3.4.3.3 Group III (Nano-FA). At 2 and 6 weeks, compared to groups I and II, it presented a socket area filled with thick bone trabeculae arising from the wall, except for a small part at week 2 and the bone marrow spaces at 6 weeks (Fig. 7 – C1 and C2).

3.4.3.4 Group IV (CS–Nano-FA–HPMC). At 2 and 6 weeks, compared to group III, nearly all the socket area was filled with thick bone trabeculae from the wall, which appeared at week 6 as compact bone formed from mixed smooth and rough surface areas with some depressions in between (Fig. 7 – D1 and D2).

3.5. Result biochemical analysis

3.5.1. Inflammatory cytokines (TNF-α and IL-1β) (Fig. 8 and Table 1)

3.5.1.1 TNF-α levels. Two weeks after tooth extraction, the −ve control group possessed the highest levels of TNF-α at 369.4 ± 22.73 pg mL^{-1}, while the CS–Nano-FA–HPMC group showed the lowest levels at 266.8 ± 20.36 pg mL^{-1}. This difference among groups was statistically significant (F = 16.698, p < 0.001). A deeper analysis confirmed that the combination treatment significantly lowered TNF-α levels when compared with both the −ve control group (p < 0.001) and the groups receiving either CS (p = 0.039) or Nano-FA (p = 0.002) alone. By six weeks, TNF-α levels had dropped significantly across all groups (p < 0.001). The CS + Nano-FA group continued to maintain the lowest levels (51.8 ± 11.80 pg mL^{-1}), exhibiting a statistically significant variation compared to the other groups (F = 41.835, p < 0.001).

3.5.1.2 IL-1β levels. A similar pattern was seen with IL-1β. At the two-week mark, the −ve control group had the highest IL-1β levels (213.6 ± 14.99 pg mL^{-1}), while the combination group (CS–Nano-FA–HPMC) showed the lowest (74.8 ± 10.28 pg mL^{-1}), with a substantial statistical difference (F = 99.075, p < 0.001). Pairwise comparisons confirmed that the combination group had significantly lower IL-1β than all other groups (p < 0.001). By six weeks, IL-1β levels had dropped further in all groups except the CS-only group, where the reduction wasn't statistically meaningful (p = 0.966). Still, the combination group had the lowest IL-1β at 49.2 ± 12.85 pg mL^{-1}, again with a significant difference across groups (F = 21.607, p < 0.001).

3.5.2. Bone remodeling markers (TGF-β1, osteocalcin, and ALP) (Fig. 8 and Table 2)

3.5.2.1 TGF-β1 levels. At two weeks, the highest TGF-β1 levels were recorded in the −ve control group (2.07 ± 0.20 ng mL^{-1}), while the combination group (CS–Nano-FA–HPMC) had the lowest (1.39 ± 0.12 ng mL^{-1}) with significant group differences (F = 15.323, p < 0.001). By six weeks, levels had decreased in all groups. Still, the combination group showed the lowest values (1.30 ± 0.13 ng mL^{-1}), remaining significantly different from the rest (F = 14.945, p < 0.001; p = 0.002 *vs.* other groups).

3.5.2.2 Osteocalcin levels. Osteocalcin, a key indicator of bone formation, was notably higher in all treatment groups than in the −ve control at both time points. At two weeks, it ranged from 23.8 ± 3.56 ng mL^{-1} in the −ve control group to 70.6 ± 7.33 ng mL^{-1} in the CS–Nano-FA–HPMC group (F = 74.830, p < 0.001). This upward trend continued at six weeks, with the combination group peaking at 80.6 ± 6.54 ng mL^{-1} (F = 106.186, p < 0.001).

3.5.2.3 Alkaline phosphatase (ALP) activity. The pattern was consistent for ALP activity. After two weeks, the CS–Nano-FA–HPMC group recorded much higher ALP levels (198.6 ± 5.13 U L^{-1}) compared to the control (101.4 ± 5.59 U L^{-1}) with a highly significant difference (F = 151.688, p < 0.001). At six weeks, ALP levels increased across all groups, and the CS–Nano-FA–HPMC group reached the highest value at 315.4 ± 11.87 U L^{-1}, significantly outperforming the others (F = 47.688, p < 0.001).

3.6. Statistical results

3.6.1. Histomorphometric results of bone surface area (Fig. 9). Table 3 and Fig. 9 display the new bone surface area percentages for all groups over the two study intervals (2 and 6 weeks). The results are summarized as the means and standard deviations. Group IV (CS–Nano-FA–HPMC) showed the highest rate of new bone formation (39.73 ± 1.07), (88.33 ± 2.78) after 2 and 6 weeks respectively, followed by group III (*Nano-FA*) (24.50 ± 1.10), (75.53 ± 4.72) then group II (CS) (18.77 ± 0.45), (66.07 ± 3.09) while group I (−ve control) exhibited the lowest percentage (11.30 ± 0.85), (31.83 ± 3.50) after 2 and 6 weeks, respectively. After weeks 2 and 6, there was a statistically significant difference in the percentage of newly formed bone between group I and the treatment groups (II, III, and IV) (p < 0.001). Moreover, at the two intervals, there was a statistically significant difference regarding the percentage of new bone among the treatment groups (II, III, and IV) (p_1 < 0.001), (p_2 < 0.001), and (p_3 < 0.001), respectively.

4. Discussion

The quality assessment and histological evaluation of the CS as an inorganic composite in alveolar socket repair are poorly understood, despite numerous biomaterials-related studies having been conducted.[53,54] Considering this, the current work

(arrow) and osteon formation inside the new bone (circled area). Also, mixed fibrous and granulation areas (star) are more easily detected in large amounts at week 2, but by week 6, only fibrous tissue (star) can be depicted. (D1 and D2) Group IV (CSNPs + Nano-FA) at 2 and 6 weeks, respectively, showing more bone formation with less fibrous tissue (star), bone remodelling lines (arrow), osteon formation (circled area), and entrapped osteocytes (curved arrow). In week 6, there is more bone formation, with an increased number of bone remodelling lines (arrow), osteon formation (circled area), and entrapped osteocytes (curved arrow) (Gomori trichrome stain X 400).

 © 2026 The Author(s). Published by the Royal Society of Chemistry

Open Access Article. Published on 04 February 2026. Downloaded on 2/26/2026 3:16:51 PM.
This article is licensed under a Creative Commons Attribution-NonCommercial 3.0 Unported Licence.

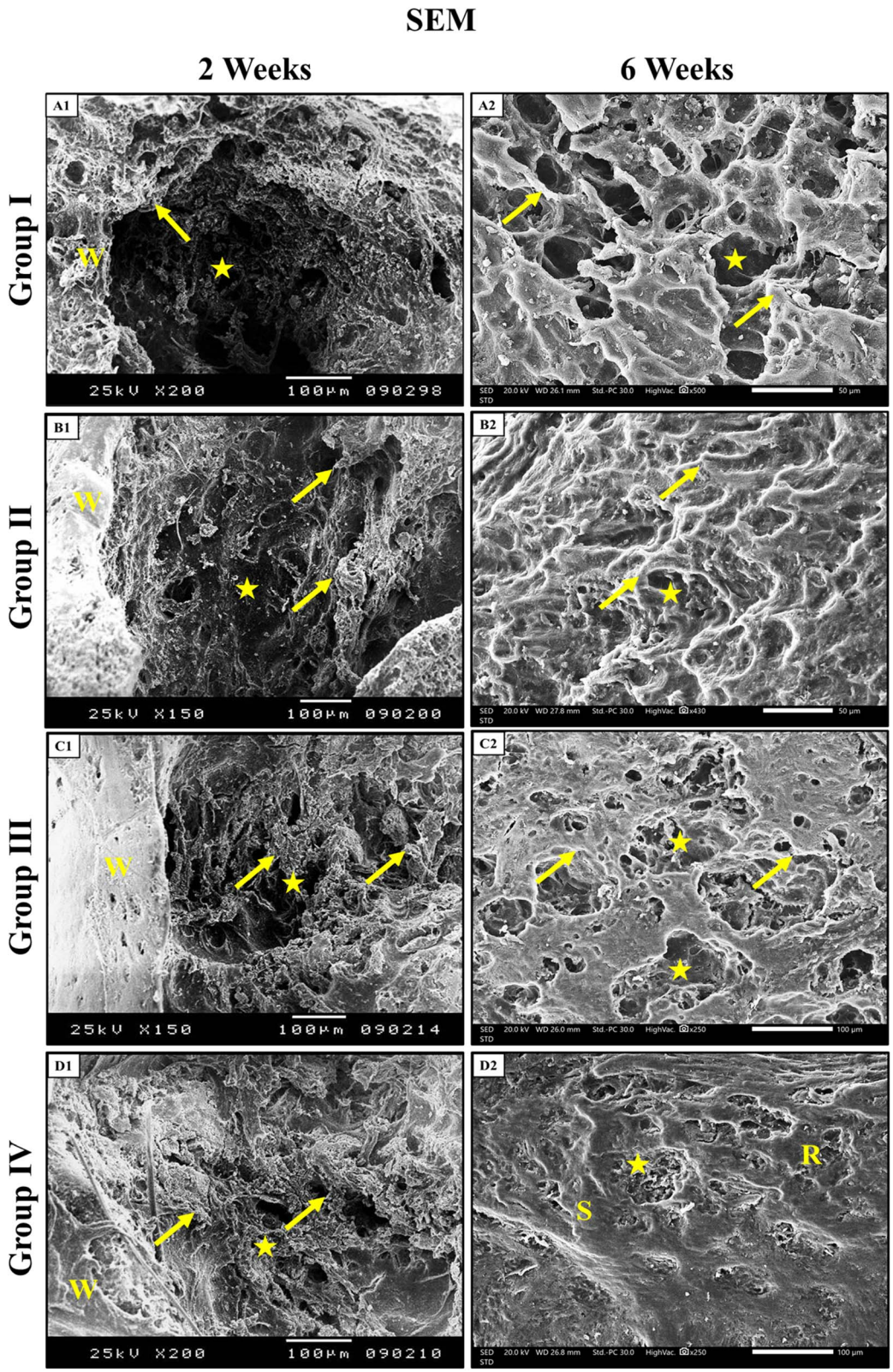

Fig. 7 Scanning electron micrographs of the socket for all groups. (A1 and A2) Group I (DM) at 2 and 6 weeks, respectively, showing a well-defined socket area (star) surrounded by the socket wall (W) with few thin short bone trabeculae (arrow) arising from the wall. At 6 weeks (A2), the thin, irregular bone trabeculae are increased in number around the wide bone marrow spaces (star). (B1 and B2) Group II (CS) at 2 and 6 weeks, respectively, showing a small socket area (star) surrounded by the socket wall (W) with thin short bone trabeculae (arrow) arising from the wall. At 6 weeks (B2), the thin bone trabeculae are increased in number around the narrow bone marrow spaces (star). (C1 and C2) Group III (Nano-FA) at 2 and 6 weeks, respectively, showing socket area filled with bone except for a small part (star), note that the socket contains thick bone trabeculae (arrow) arising from the wall (W). At 6 weeks (C2), the bone trabeculae filled the socket area except at the bone marrow spaces (star).

Open Access Article. Published on 04 February 2026. Downloaded on 2/26/2026 3:16:51 PM.
This article is licensed under a Creative Commons Attribution-NonCommercial 3.0 Unported Licence.

aims to determine the osteogenic properties of CS, Nano-FA, and their combinations in CS–Nano-FA–HPMC paste on bone regeneration and healing following tooth extraction in diabetic rat models.

Notably, we selected the mandibular first molars because they are the most prominent teeth in the rodent dentition and provide well-defined sockets that allow consistent surgical procedures and reliable post-extraction assessment.[54] Bilateral extraction was performed as no previous studies have shown anatomical or biological distinctions in healing patterns between the left and right mandibular molar sockets in rats. Also, we examined the right-side sockets by SEM to maintain methodological consistency across samples and reduce processing variability. The left-side sockets were prepared for LM evaluations. Healing sequelae are affected by DM, which impairs blood circulation, lowers the immunological response, and delays tissue regeneration, as in tooth socket recovery after extraction.[55] The most crucial point is that uncontrolled DM compromises the immune system, decreasing the efficiency of immune cells, and may increase the risk of dry socket after extraction.[56] In addition, hyperglycemia developed from DM hampered angiogenesis and collagen-scaffolded formation during tissue regeneration.[57] Thus, dentists should confirm the blood glucose level and prove that DM is controlled before extraction.[58] In some cases, DM is difficult to control, as in the case of obese patients consuming poor diets, a lack of physical activity, and patients under stress.[59,60]

To assess the long-term effects of DM on the regeneration of bone in extraction sockets, diabetic rats were selected to undergo tooth extraction at intervals of 2 and 6 weeks. In comparison, 2 weeks were needed to evaluate the initial healing and inflammation, and 6 weeks were required to assess the formation and development of the bone tissue in the socket.[61] Histological assessment included staining with H&E to analyze bone regeneration and with Masson trichrome to evaluate collagen formation.[34] Similarly, rat sockets were assessed using SEM to investigate the superficial morphology of the bone following the application of the materials.[64]

CS–Nano-FA may provide distinct benefits compared to CS–Nano-HA in healing extraction sockets in diabetic rat models. The rationale is that incorporating fluoride into the apatite lattice results in lower solubility in acidic environments, leading to prolonged structural stability in inflamed or diabetic tissues, where the local pH may be compromised. This could potentially offer prolonged structural support during bone regeneration.[62] Moreover, FA has been shown to suppress osteoclastic bone resorption, a feature of relevance in diabetic conditions, where bone turnover is often impaired.[63] Also, hydroxypropyl methylcellulose (HPMC) was used as the paste-making agent in the formulation due to its favorable physicochemical and rheological properties. Its compatibility with polysaccharide-based systems allows for the formation of a stable, cohesive gel with CS, as reported by Yu *et al.*[43] Blending HPMC with hydroxypropyl starch (HPS) has enhanced mechanical strength and barrier function while minimizing moisture diffusion from the surrounding area.

Histologically, as depicted in H&E, Masson trichrome, and SEM results, the granulation tissue, comprising collagen, tiny blood vessels, and fibroblasts, developed in all groups with varying amounts between weeks 2 and 6. It is an essential component of the initial healing response, as a foundation for later bone repair.[64] *In group I (DM)*, bone development has significantly increased at 6 weeks. Thinner bone trabeculae were formed, and the granulation tissue became less noticeable. Furthermore, bone resting lines, which indicate the development of new bone layers and the advancement of bone remodeling, become more evident. This transition is apparent from the granulation tissue, which represents the initial phase of inflammation, to a more regenerative phase characterized by increased bone production.[65,66] Additionally, within group II (CS), CS appeared to promote effective bone regeneration. Granulation tissue and the development of bones were signs of early healing observed at week 2. In contrast, by week 6, a notable presence of mature bone was observed, accompanied by a decrease in granulation tissue and evidence of active remodeling. CS contributes to bone repair by encouraging the proper transition of tissue from inflammation to maturation.[69] Nevertheless, in the present investigation, the application of CS hydrogel in the extraction socket failed to achieve adequate bone regeneration after a 6 week healing interval. These observations align with earlier studies demonstrating limited osteogenic outcomes when chitosan (CS) is used solely as a scaffold material.[70] Notably, the degree of deacetylation and the molecular weight are significant parameters of CS. As a result, the chitosan used in this study exhibited a considerable degree of deacetylation, which facilitated its degradation rate. Still, it failed to adequately sustain the whole regenerative process over the full period of bone remodeling. Li *et al.*[71] concluded that CS created a cell-friendly environment that facilitated the rapid infiltration and healing of the extraction wound. Still, it did not provide sufficient structural integrity to support robust bone formation in critical-sized defects, such as extraction sockets. *In group III (Nano-FA)*, more osteocytes were incorporated into the new bone structure over 2 to 6 weeks, and increased activity indicates bone remodeling and healing. However, it did not result in appropriate bone regeneration after a 6 week healing interval. This finding is consistent with earlier research by Zeng *et al.*,[67] which found that although Nano-FA has good bioactivity *in vitro*, its *in vivo* osteogenic potential is frequently limited. It lacks the biological climate required for osteoblast adhesion and migration. Nonetheless, *in group IV (CS–Nano-FA–HPMC)*, at 2 and 6 weeks, compared to

(D1 and D2) Group IV (CS + Nano-FA) at 2 and 6 weeks, respectively, showing nearly all the socket area filled with bone (star), note that the socket contains thick bone trabeculae (arrow) arising from the wall (W). At 6 weeks (D2), the bone trabeculae filled the socket area, and mixed smooth (S) and rough (R) surface areas appeared with some depressions (star) in between (SEM, original magnification; (A1 and D1) ×200; (B1 and C1) ×150; (A2) ×500; (B2) ×430; (C2 and D2) ×250).

 © 2026 The Author(s). Published by the Royal Society of Chemistry

Open Access Article. Published on 04 February 2026. Downloaded on 2/26/2026 3:16:51 PM.
This article is licensed under a Creative Commons Attribution-NonCommercial 3.0 Unported Licence.

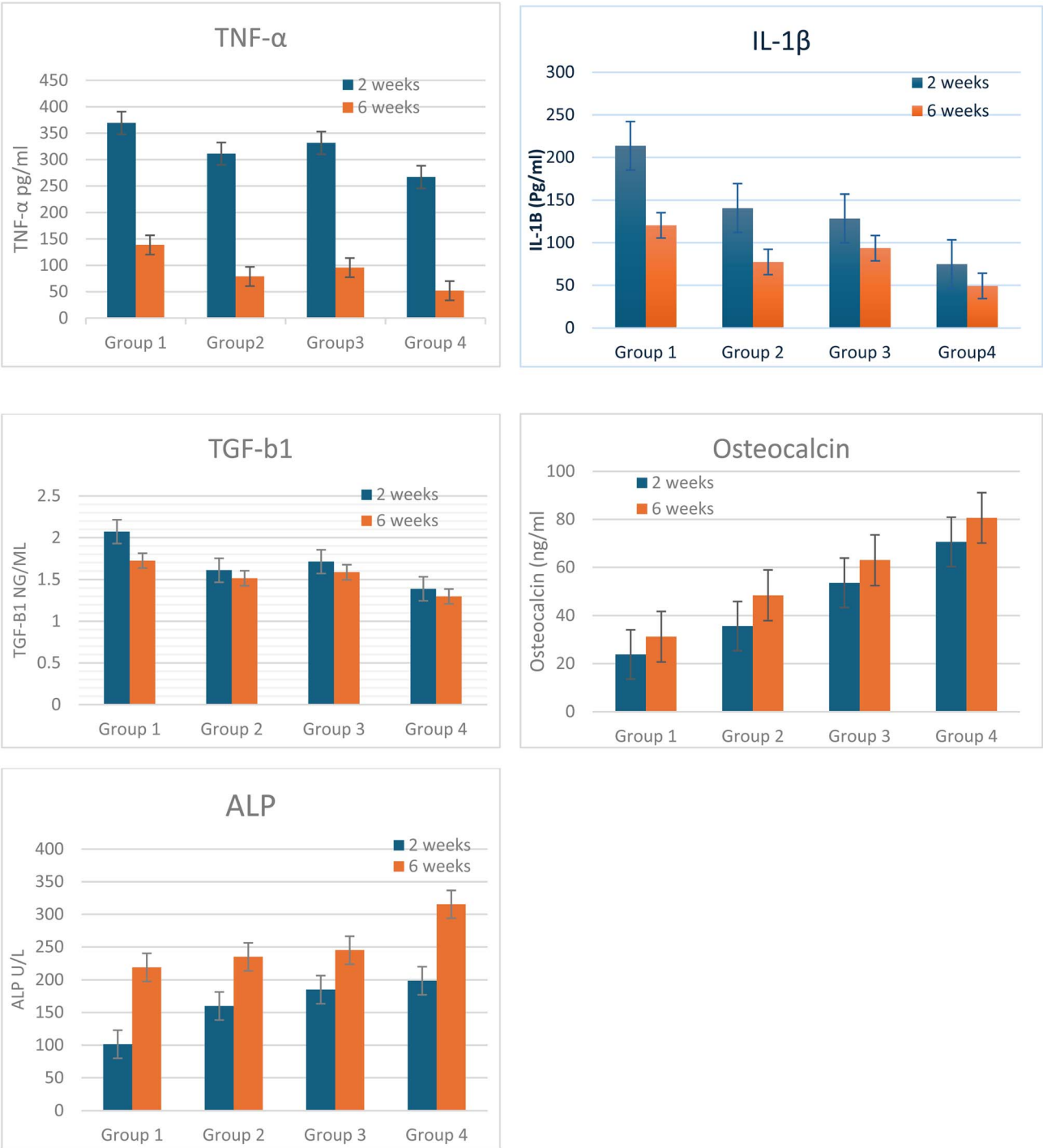

Fig. 8 Comparison between the different studied groups according to TNF-alpha, IL-1β, TGF-β1, osteocalcin, and ALP over the two intervals, 2 and 6 weeks, respectively, Group I (DM, Group II (CS)), Group III (Nano-FA), and Group IV (CS + Nano-FA).

group III, there was an increase in trabecular bone formation, accompanied by a reduction in fibrous tissue and fewer bone remodeling lines. By week 6, bone formation was more pronounced, with more bone remodeling lines and entrapped osteocytes. The entire socket area was filled with thick bone trabeculae extending from the wall.

The statistical evaluation of the histomorphometric results for bone surface area was consistent with the histological findings. As group IV (CS–Nano-FA–HPMC) showed the highest rate of new bone formation after both 2 and 6 weeks, followed by group III (Nano-FA), then group II (CS), group I (−ve control) showed the lowest new bone area percentage after 2 and 6 weeks, respectively. After weeks 2 and 6, there was a statistically

Open Access Article. Published on 04 February 2026. Downloaded on 2/26/2026 3:16:51 PM.
This article is licensed under a Creative Commons Attribution-NonCommercial 3.0 Unported Licence.

Table 1 Comparison between the different studied groups according to TNF-alpha and IL-1β B[a]

		D + Ext. teeth	CS	Nano-FA	CS–Nano-FA–HPMC	F	p
TNF-alpha (pg ml^{-1})	**After two weeks**						
	Min.–Max.	340–390	285–350	290–350	240–288	16.698	<0.001*
	Mean ± SD.	369.4 ± 22.73	311^{a} ± 26.08	331.4 ± 24.02	266.8^{abc} ± 20.36		
	p_0		0.006*	0.087	<0.001*		
	Sig. bet. Grps.		$p_1 = 0.529$, $p_2 = 0.039$*, $p_3 = 0.002$*				
	After 6 weeks						
	Min.–Max.	115–156	65–90	84–110	42–72	41.835*	<0.001*
	Mean ± SD.	138.6 ± 16.40	78.80^{a} ± 10.13	95.60^{a} ± 11.06	51.80^{abc} ± 11.80		
	p_0		<0.001*	<0.001*	<0.001*		
	Sig. bet. Grps.		$p_1 = 0.191$, $p_2 = 0.018$*, $p_3 < 0.001$*				
	p_4	<0.001*	<0.001*	<0.001*	<0.001*		
IL-1B (pg ml^{-1})	**After two weeks**						
	Min.–Max.	190–230	73–100	100–145	61–86	99.075*	<0.001*
	Mean ± SD.	213.6 ± 14.99	88^{a} ± 10.70	128.4 ^{ab} ± 18.58	74.80^{ac} ± 10.28		
	p_0		<0.001*	<0.001*	<0.001*		
	Sig. bet. Grps.		$p_1 = 0.002$*, $p_2 = 0.469$, $p_3 < 0.001$*				
	After 6 weeks						
	Min.–Max.	90–147	73–100	82–100	31–65	21.607*	<0.001*
	Mean ± SD.	120.4 ± 21.52	88.40^{a} ± 10.83	93.60^{a} ± 7.23	49.20^{abc} ± 12.85		
	p_0		0.012*	0.038*	<0.001*		
	Sig. bet. Grps.		$p_1 = 0.936$, $p_2 = 0.002$*, $p_3 = 0.001$*				
	p_4	0.001*	0.966	0.028*	0.009*		

[a] SD: standard deviation, a: significant with group 1, b: significant with CS, c: significant with Nano-FA. F: F for one-way ANOVA test, pairwise comparison between. Each of the 2 groups was done using the *post hoc* test (Tukey). p: p-value for comparing between the studied groups. p_0: p value for comparing between D + Ext. teeth and each other group. p_1: p-value for comparing between Chit and Nano-FA. p_2: p-value for comparing between CS and CS–Nano-FA–HPMC. p_3: p-value for comparing between Nano-FA and CS–Nano-FA–HPMC. p_4: p-value for Paired t-test for comparing between after two weeks and after 6 weeks in each group. *Statistically significant at $p \leq 0.05$.

significant difference in the rate of newly formed bone between group I and the treatment groups (II, III, and IV). Moreover, at both intervals, there was a statistically significant difference in the percentage of new bone among the treatment groups (II, III, and IV). When Nano-FA was used alone as a graft biomaterial inside the alveolar socket of diabetic rats, it didn't produce sufficient bone regeneration. This is despite Nano-FA being known for having better mechanical strength and a slower rate of degradation than HA, which can promote osteoblast proliferation and mineral deposition.[67] On the other hand, the combination of Nano-FA with CS produced better histological results. The probable reason for this was the synergistic effect of the two substances: Nano-FA contributed to mineralization and osteoconductivity, whereas CS supplies a biocompatible and biodegradable matrix that enhances cell migration, adhesion, proliferation, and differentiation.[67] The CS matrix could also facilitate a more even dispersion of the Nano-FA and prevent their aggregation, which ensures sustained ionic release and improved functionality of the extraction socket.[68] A study that implemented a CS-HA scaffold for periodontal regeneration reported an increase in new bone production.[69] Their outcomes highlighted the significance of CS in regulating the degradation profile and bio-distribution of Nano-HA to remedy bone deficiencies in low-load-bearing areas, which encompass peri-implant and periodontal regenerative procedures.

Inflammatory markers in groups treated with CS (Group II), Nano-FA (Group III), and particularly CS–Nano-FA–HPMC (Group IV) revealed a substantial decline in TNF-α and IL-1β levels compared to the untreated diabetic group (Group I). This aligns with previous studies, which have shown that CS exhibits potent anti-inflammatory properties by inhibiting pro-inflammatory cytokines. For example, some studies reported reduced TNF-α and IL-1β expression in inflamed tissues treated with CS scaffolds.[63] Likewise, Li *et al.*[71] found that CS reduced inflammatory cytokine production in diabetic wound healing models. Nano-FA also played a role in the anti-inflammatory response, probably by creating a conducive microenvironment for tissue regeneration. *TGF-β1 modulation*: In all groups, TGF-β1 levels decreased from week 2 to week 6, which aligns with the expected biological progression from the proliferative phase to the remodeling phase of wound healing. The most substantial decline was observed in group IV, suggesting accelerated tissue maturation. These results are supported by research from Elimelech *et al.*,[72] who found that TGF-β1 expression was modulated more effectively with the application of a bioactive scaffold in bone regeneration.

Bone regeneration markers: Osteocalcin and ALP levels elevated over time in all groups, with the highest values consistently detected in group IV. This suggests that combining CS and Nano-FA improves osteoblastic activity and matrix mineralization. These results agree with earlier reports highlighting the osteoinductive potential of CS and nano-hydroxyapatite combinations. According to Chesnutt *et al.*,[73] CS–Nano-HA composites considerably upregulated ALP activity and osteocalcin expression *in vitro* and *in vivo*. Another study

 © 2026 The Author(s). Published by the Royal Society of Chemistry

Open Access Article. Published on 04 February 2026. Downloaded on 2/26/2026 3:16:51 PM.
This article is licensed under a Creative Commons Attribution-NonCommercial 3.0 Unported Licence.

Table 2 Comparison between the different studied groups according to TGF-β1, osteocalcin, and ALP[a]

		D + Ext. teeth	CS	Nano-FA	CS–Nano-FA–HPMC	F	p
TGF-b1 (ng ml^{-1})	**After two weeks**						
	Min.–Max.	1.84–2.34	1.32–1.77	1.52–1.83	1.22–1.55	15.323*	<0.001*
	Mean ± SD.	2.07 ± 0.20	1.61^{a} ± 0.18	1.71^{a} ± 0.13	1.39^{ac} ± 0.12		
	p_0		0.002*	0.014*	<0.001*		
	Sig. bet. Grps.		$p_1 = 0.757$, $p_2 = 0.178$, $p_3 = 0.029$*				
	After 6 weeks						
	Min.–Max.	1.64–1.85	1.42–1.61	1.43–1.72	1.11–1.46	14.945*	<0.001*
	Mean ± SD.	1.72 ± 0.08	1.51 ± 0.08	1.59 ± 0.11	1.30^{abc} ± 0.13		
	p_0		0.024*	0.188	<0.001*		
	Sig. bet. Grps.		$p_1 = 0.691$, $p_2 = 0.020$*, $p_3 = 0.002$*				
	p_4	0.029*	0.306	0.047*	0.151		
Osteocalcin	**After two weeks**						
	Min.–Max.	20–28	31–40	45–61	62–78	74.830*	<0.001*
	Mean ± SD.	23.80 ± 3.56	35.60^{a} ± 3.51	53.60 ^{ab} ± 5.81	70.60^{abc} ± 7.33		
	p_0		0.014*	<0.001*	<0.001*		
	Sig. bet. Grps.		$p_1 < 0.001$*, $p_2 < 0.001$*, $p_3 = 0.001$*				
	After 6 weeks						
	Min.–Max.	28–35	45–51	58–71	72–88	106.186*	<0.001*
	Mean ± SD.	31.20 ± 2.86	48.40^{a} ± 2.41	63 ^{ab} ± 5.15	80.60^{abc} ± 6.54		
	p_0		<0.001*	<0.001*	<0.001*		
	Sig. bet. Grps.		$p_1 = 0.001$*, $p_2 < 0.001$*, $p_3 < 0.001$*				
	p_4	0.013*	0.005*	0.095	0.081		
ALP	**After two weeks**						
	Min.–Max.	95–109	149–173	174–197	192–205	151.688*	<0.001*
	Mean ± SD.	101.4 ± 5.59	160^{a} ± 9.87	185 ^{ab} ± 9.41	198.6^{abc} ± 5.13		
	p_0		<0.001*	<0.001*	<0.001*		
	Sig. bet. Grps.		$p_1 = 0.001$*, $p_2 < 0.001$*, $p_3 = 0.061$				
	After 6 weeks						
	Min.–Max.	202–231	210–260	236–255	300–332	47.688*	<0.001*
	Mean ± SD.	219 ± 12.69	235 ± 20	245.2^{a} ± 7.60	315.4^{abc} ± 11.87		
	p_0		0.293	0.038*	<0.001*		
	Sig. bet. Grps.		$p_1 = 0.653$, $p_2 < 0.001$*, $p_3 < 0.001$*				
	p_4	<0.001*	0.001*	<0.001*	<0.001*		

[a] SD: standard deviation, a: significant with group 1, b: significant with CS, c: significant with Nano-FA. F: F for One-way ANOVA test, pairwise comparison between. Each of the 2 groups was done using the *post hoc* test (Tukey). p: p-value for comparing between the studied groups. p_0: p value for comparing between D + Ext. teeth and each other group. p_1: p-value for comparing between Chit and Nano-FA. p_2: p-value for comparing between CS and CS–Nano-FA–HPMC. p_3: p-value for comparing between Nano-FA and CS–Nano-FA–HPMC. p_4: p-value for paired t-test for comparing between after two weeks and after 6 weeks in each group. *Statistically significant at $p \leq 0.05$.

Table 3 Comparison between all groups regarding the percentage of surface area of the newly formed bone over the two intervals, 2 and 6 weeks

Percentage of new bone	Group I (DM) ($n = 10$)	Group II (CSNPs) ($n = 10$)	Group III (nano-FA) ($n = 10$)	Group IV (CSNPs + nano-FA) ($n = 10$)	F	p
Week 2 ($n = 5$)						
Min.–Max.	10.50–12.20	18.30–19.20	23.40–25.60	38.80–40.90	530.316*	**<0.001***
Mean ± SD.	11.30 ± 0.85	18.77 ± 0.45	24.50 ± 1.10	39.73 ± 1.07		
Median	11.20	18.80	24.50	39.50		
$p_{control}$		<0.001*	<0.001*	<0.001*		
Sig. bet. grps		$p_1 < 0.001$*, $p_2 < 0.001$*, $p_3 < 0.001$*				
Week 6 ($n = 5$)						
Min.–Max.	29.20–35.80	63.30–69.40	70.10–78.60	85.20–90.50	135.704*	**<0.001***
Mean ± SD.	31.83 ± 3.50	66.07 ± 3.09	75.53 ± 4.72	88.33 ± 2.78		
Median	30.50	65.50	77.90	89.30		
$p_{control}$		<0.001*	<0.001*	<0.001*		
Sig. bet. grps		$p_1 = 0.001$*, $p_2 < 0.001$*, $p_3 = 0.001$*				

Open Access Article. Published on 04 February 2026. Downloaded on 2/26/2026 3:16:51 PM.
This article is licensed under a Creative Commons Attribution-NonCommercial 3.0 Unported Licence.

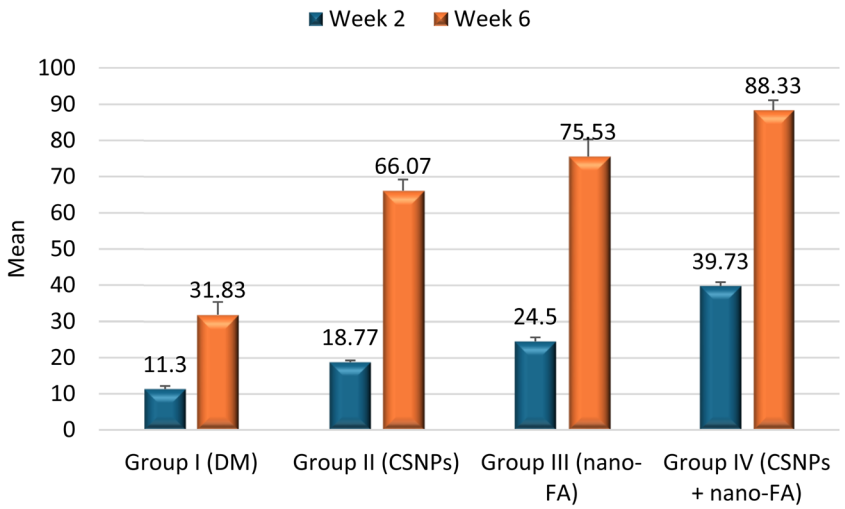

Fig. 9 Bar chart comparing all groups regarding the percentage of newly formed bone surface area over the two intervals, 2 and 6 weeks, respectively.

reported improved bone formation in diabetic rat models treated with CS and HA blends.[74]

Thus, the synergistic effect observed in group IV likely stems from the complementary actions of CS and Nano-FA. CS provides antibacterial, anti-inflammatory, and matrix-stabilizing functions, while Nano-FA contributes to osteoconduction and mineralization. Together, they create a bioactive scaffold that reduces inflammation and supports robust bone regeneration.[74]

5. Conclusion

According to the histological and biochemical exploration, the current study's findings showed that although CS and Nano-FA had beneficial osteoconductive qualities, they did not promote bone formation as much as the novel CS–Nano-FA–HPMC paste. CS supports anti-inflammatory responses and regenerative processes, promoting angiogenesis and tissue repair, which are often impaired in diabetic conditions. The regeneration pattern shown in the histomorphometric results further supports this.

6. Recommendation

Although the benefits of the suggested hydrogel in this work are promising, assessing its effectiveness in larger animal models is still necessary to more accurately research the clinical use of CS–Nano-FA–HPMC scaffolds in bone regeneration.

7. Study limitations

While this study focused on histological and ultrastructural analysis of bone socket healing in diabetic rats, future research should consider analyzing additional markers to provide a molecular overview of this process and further exploring any systemic effects of the Nano-FA and CS–Nano-FA–HPMC nanocomposite. The SEM-based microstructural evaluation in this work was performed as a qualitative confirmatory tool to support the physicochemical analyses rather than as a quantitative porosity evaluation approach. Although quantitative pore-network measurements (*e.g.*, μ-CT stereology) were beyond the scope of the present biologically-focused investigation, future work will incorporate these analyses to further correlate scaffold architecture with tissue-level regenerative outcomes. In addition, while histological and SEM analysis provide corresponding data at the cellular and surface levels, they are limited to two-dimensional sections. Micro-CT minimizes these limitations, providing a more objective assessment of overall bone healing. Incorporating immunohistochemistry (IHC) or immunofluorescence (IF) to visualize key osteogenic markers (*e.g.*, Runx2, OCN, ALP) would indeed provide more direct evidence of protein-level changes in bone healing.

Author contributions

Rehab M. El-Sharkawy: methodology, conceptualization, data curation, investigation, visualization, formal analysis, writing – original draft, writing – review & editing. Eman M. Salem: methodology, conceptualization, data curation, investigation, visualization, formal analysis, writing – review & editing. Rania A. Hanafy: methodology, conceptualization, data curation, investigation, formal analysis, visualization, writing – original draft, writing – review & editing. Nevien. M. Ahmed: methodology, conceptualization, data curation, investigation, visualization, formal analysis, writing – original draft, writing – review & editing. Omnia M. Abdelfatah: data curation, methodology. Wafaa Yahia Alghonemy: methodology, conceptualization, data curation, investigation, visualization, formal analysis, writing – original draft, writing – review & editing. All the authors reviewed the results and approved the final version of the manuscript.

 © 2026 The Author(s). Published by the Royal Society of Chemistry

Open Access Article. Published on 04 February 2026. Downloaded on 2/26/2026 3:16:51 PM.
This article is licensed under a Creative Commons Attribution-NonCommercial 3.0 Unported Licence.

Conflicts of interest

The authors declare no conflicts of interest relevant to this article.

Data availability

On reasonable request, the datasets utilized and analyzed during the present study are accessible from the corresponding author.

Acknowledgements

The authors cordially acknowledge Prof. Yosra S. R. Elnaggar, Head of Research & International Publishing Administration (RIPA) at Pharos University in Alexandria, for assistance in the international publishing process.

References

1 P. Li, K. K. K. Alenazi, J. Dally, E. L. Woods, R. J. Waddington and R. Moseley, Role of oxidative stress in impaired type II diabetic bone repair: scope for antioxidant therapy intervention?, *Front. Dent. Med.*, 2024, **5**, 1464009, DOI: 10.3389/fdmed.2024.1464009.

2 S. Yang, Y. Li, C. Liu, Y. Wu, Z. Wan and D. Shen, Pathogenesis and treatment of wound healing in patients with diabetes after tooth extraction, *Front. Endocrinol.*, 2022, **13**, 949535, DOI: 10.3389/fendo.2022.949535.

3 C. Shi, Z. Yuan, F. Han, C. Zhu and B. Li, Polymeric biomaterials for bone regeneration, *Ann. Jt.*, 2016, **1**, 1–27.

4 V. Campana, G. Milano, E. Pagano, M. Barba, C. Cicione, G. Salonna, W. Lattanzi and G. Logroscino, Bone substitutes in orthopaedic surgery: from basic science to clinical practice, *J. Mater. Sci. Mater. Med.*, 2014, **25**, 2445–2461.

5 E. Wahjuningsih and S. Sularsih, Expression of bone morphogenetic protein-2 after using chitosan gel with different molecular weight on wound healing process of dental extraction, *Dental Journal (Majalah Kedokteran Gigi)*, 2015, **48**, 53–58.

6 Z. Zou, L. Wang, Z. Zhou, Q. Sun, D. Liu, Y. Chen, H. Hu, Y. Cai, S. Lin and Z. Yu, Simultaneous incorporation of PTH (1–34) and nano-hydroxyapatite into Chitosan/Alginate Hydrogels for efficient bone regeneration, *Bioact. Mater.*, 2021, **6**, 1839–1851.

7 S. K. L. Levengood and M. Zhang, Chitosan-based scaffolds for bone tissue engineering, *J. Mater. Chem. B*, 2014, **2**, 3161–3184.

8 S. Afra, M. Koch, J. Żur-Pińska, M. Dolatshahi, A. R. Bahrami, J. E. Sayed, A. Moradi, M. M. Matin and M. K. Włodarczyk-Biegun, Chitosan/Nanohydroxyapatite/Hydroxyethyl-cellulose-based printable formulations for local alendronate drug delivery in osteoporosis treatment, *Carbohydr. Polym. Technol. Appl.*, 2024, **7**, 100418.

9 M. Jahangirnezhad, I. Kazeminezhad, G. Saki, S. Amirpoor and M. Larki, The effects of Nanohydroxyapatite on bone regeneration in rat calvarial defects, *Am. J. Res. Commun.*, 2013, **1**, 302–316.

10 H. Zhou and J. Lee, Nanoscale hydroxyapatite particles for bone tissue engineering, *Acta Biomater.*, 2011, **7**, 2769–2781.

11 L. Canullo, C. Dellavia and F. Heinemann, Maxillary sinus floor augmentation using a nano-crystalline hydroxyapatite silica gel: case series and 3-month preliminary histological results, *Ann. Anat.*, 2012, **194**, 174–178.

12 L. Borkowski, A. Przekora, A. Belcarz, K. Palka, G. Jozefaciuk, T. Lübek, M. Jojczuk, A. Nogalski and G. Ginalska, Fluorapatite ceramics for bone tissue regeneration: Synthesis, characterization and assessment of biomedical potential, *Mater. Sci. Eng., C*, 2020, **116**, 111211.

13 L. Borkowski, A. Przekora, A. Belcarz, K. Palka, M. Jojczuk, P. Lukasiewicz, A. Nogalski and G. Ginalska, Highly porous fluorapatite/β-1, 3-glucan composite for bone tissue regeneration: Characterization and in-vitro assessment of biomedical potential, *Int. J. Mol. Sci.*, 2021, **22**, 10414.

14 E. M. Salem, O. M. Abdelfatah, R. A. Hanafy, R. M. El-Sharkawy, G. Elnawawy and W. Y. Alghonemy, Comparative study of pulpal response following direct pulp capping using synthesized fluorapatite and hydroxyapatite nanoparticles, *BMC Oral Health*, 2025, **25**, 17.

15 H.-P. Yu and Y.-J. Zhu, Guidelines derived from biomineralized tissues for design and construction of high-performance biomimetic materials: from weak to strong, *Chem. Soc. Rev.*, 2024, **53**, 4490–4606.

16 S. Song, J. Ni, Y. Sun, Q. Pu, L. Zhang, Q. Yan and J. Yu, Association of inflammatory cytokines with type 2 diabetes mellitus and diabetic nephropathy: a bidirectional Mendelian randomization study, *Front. Med.*, 2024, **11**, 1459752.

17 O. M. Abd El Fatah, S. Abd El Samad, A. Koura and D. A. Nagy, Scanning electron microscopic evaluation of the effect of boron and fish oil on healing of extraction sockets in rats, *Alex. Dent. J.*, 2020, **45**, 117–124.

18 J. Charan and T. Biswas, How to calculate sample size for different study designs in medical research?, *Indian J. Psychol. Med.*, 2013, **35**, 121–126.

19 H. G. C. Van Spall, A. Toren, A. Kiss and R. A. Fowler, Eligibility criteria of randomized controlled trials published in high-impact general medical journals: a systematic sampling review, *JAMA, J. Am. Med. Assoc.*, 2007, **297**, 1233–1240.

20 F. Faul, E. Erdfelder, A.-G. Lang and A. Buchner, G* Power 3: A flexible statistical power analysis program for the social, behavioral, and biomedical sciences, *Behav. Res. Methods*, 2007, **39**, 175–191.

21 M. D. E. Goodyear, K. Krleza-Jeric and T. Lemmens, The declaration of Helsinki, *BMJ*, 2007, **335**, 624–625.

22 E. Özkan, M. C. Bereket, M. E. Önger and A. V. Polat, The effect of unfocused extracorporeal shock wave therapy on bone defect healing in diabetics, *J. Craniofac. Surg.*, 2018, **29**, 1081–1086.

23 A. Al Shoyaib, S. R. Archie and V. T. Karamyan, Intraperitoneal route of drug administration: should it be

Open Access Article. Published on 04 February 2026. Downloaded on 2/26/2026 3:16:51 PM.
This article is licensed under a Creative Commons Attribution-NonCommercial 3.0 Unported Licence.

used in experimental animal studies?, *Pharm. Res.*, 2020, **37**, 12.

24 G. Lodi, L. Azzi, E. M. Varoni, M. Pentenero, M. Del Fabbro, A. Carrassi, A. Sardella and M. Manfredi, Antibiotics to prevent complications following tooth extractions, *Cochrane Database Syst. Rev.*, 2021, **2**, CD003811.

25 A. Moghadam, N. Moghadam, V. Doremami, S. Pishghadam and A. Mafi, A New Experimental Technique for Complete Extraction of Mandibular First Molar Teeth in Rats, *J. Vet. Dent.*, 2024, **41**, 288–292.

26 I. Binderman, G. Hallel, C. Nardy, A. Yaffe and L. Sapoznikov, A novel procedure to process extracted teeth for immediate grafting of autogenous dentin, *J. Interdiscipl. Med. Dent. Sci.*, 2014, **2**, 154.

27 Z. Lu, L. Zou, X. Zhou, D. Huang and Y. Zhang, High strength chitosan hydrogels prepared from NaOH/urea aqueous solutions: the role of thermal gelling, *Carbohydr. Polym.*, 2022, **297**, 120054.

28 N. Y. Elmehbad, N. A. Mohamed, N. A. Abd El-Ghany and M. M. Abdel-Aziz, Reinforcement of the antimicrobial activity and biofilm inhibition of novel chitosan-based hydrogels utilizing zinc oxide nanoparticles, *Int. J. Biol. Macromol.*, 2023, **246**, 125582.

29 V. Rudraradhya, B. V. Teja and D. Mukherjee, Hydroxypropyl methylcellulose/sodium alginate/hydroxyapatite nano biomaterial enriched with zinc to promote bone tissue augmentation, *J. Mol. Struct.*, 2024, **1310**, 138282.

30 S. Parasuraman, R. Raveendran and R. Kesavan, Blood sample collection in small laboratory animals, *J. Pharmacol. Pharmacother.*, 2010, **1**, 87–93, DOI: 10.4103/0976-500X.72350.

31 Y. K. Chan, P. F. Davis, S. D. Poppitt, X. Sun, N. S. Greenhill, R. Krishnamurthi, A. Przepiorski, A. T. McGill and G. W. Krissansen, Influence of tail versus cardiac sampling on blood glucose and lipid profiles in mice, *Lab. Anim.*, 2012, **46**, 142–147, DOI: 10.1258/la.2011.011136.

32 R. D. Cardiff, C. H. Miller and R. J. Munn, Manual hematoxylin and eosin staining of mouse tissue sections, *Cold Spring Harb. Protoc.*, 2014, **2014**, 655–658, DOI: 10.1101/pdb.prot073411.

33 H. S. Chae, H. Choi, I. Park, Y.-S. Moon and D.-S. Sohn, Comparative histomorphometric analysis of bone regeneration according to bone graft type, *Int. J. Oral Maxillofac. Implants*, 2023, **38**, 1191–1199.

34 E. M. Salem, R. M. El-Sharkawy, W. Y. Alghonemy, O. M. Abdelfatah and R. A. Hanafy, Alveolar bone regeneration using sustainable eggshell-derived nano-hydroxyapatite and zinc oxide nanoparticles: an in vivo experimental study, *Sci. Rep.*, 2025, **15**, 40401.

35 A. A. R. Mohammed, W. Y. Alghonemy, N. I. Sarhan, A. Abdal-Hay and R. G. Saleh, An in vivo comparative study of pure Mg and Mg-Zn alloy plates implanted in the mandible of New Zealand rabbits, *J. Oral Biol. Craniofac. Res.*, 2025, **15**, 1279–1290.

36 H. A. Shawky and D. Hassouna, Evaluation of the Regenerative Effect of Rabbit BMMSCs and ADSCs. An In Vivo Study, *Ain Shams Dent. J.*, 2021, **24**, 72–86.

37 S. W. Lee, Methods for testing statistical differences between groups in medical research: statistical standard and guideline of Life Cycle Committee, *Life Cycle 2*, 2022, e1.

38 L. Zhang, X. Bai, Y. Liang, G. Zhang, J. Zou, W. Lai and P. Fei, Preparation of chitosan derivatives/oxidized carboxymethyl cellulose hydrogels by freeze-thaw method: Synthesis, characterization, and utilization in dye absorption, *Int. J. Biol. Macromol.*, 2024, **282**, 136924.

39 A. Rahmatpour and A. H. A. Hesarsorkh, Chitosan and silica nanoparticles-modified xanthan gum-derived bio-nanocomposite hydrogel film for efficient uptake of methyl orange acidic dye, *Carbohydr. Polym.*, 2024, **328**, 121721.

40 K. Shahzad, M. A. Raza, A. Hussain, K.-C. Ko, H.-J. Jeong, K.-K. Seralathan, S. S. Han and S. H. Park, Synthesis and characterization of self-crosslinked carboxymethyl chitosan-based hydrogel and its composites with gelatin and PEG-GO for drug delivery applications, *Int. J. Biol. Macromol.*, 2025, **308**, 142256.

41 A. Jamjoom and R. E. Cohen, Grafts for ridge preservation, *J. Funct. Biomater.*, 2015, **6**, 833–848.

42 Y. Moayedee, I. Mobasherpour, S. Banijamali, M. Razavi and N. Nezafati, Effect of the nano-fluorapatite ceramic particles on mechanical behavior of fluoride varnishes, *Mater. Chem. Phys.*, 2022, **288**, 126421.

43 X. Yu, Y. Yang, Q. Liu, Z. Jin and A. Jiao, A hydroxypropyl methylcellulose/hydroxypropyl starch nanocomposite film reinforced with chitosan nanoparticles encapsulating cinnamon essential oil: Preparation and characterization, *Int. J. Biol. Macromol.*, 2023, **242**, 124605.

44 C. Tang, Y. Xu, Y. Xie, X. Liu, Z. Wang, H. Zhou, K. Cai and B. Xu, Mechanisms of gel formation in collagen/hydroxypropyl methylcellulose aqueous mixtures below the threshold for macroscopic phase separation, *Int. J. Biol. Macromol.*, 2025, **308**, 142407.

45 L. Zhang, Y. Q. Lu, Y. L. Peng, Y. X. Yu, Y. Zhao, Y. Ma and J. Y. Qian, Microstructures and properties of photophobic films composed of hydroxypropyl methylcellulose and different salts, *Int. J. Biol. Macromol.*, 2018, **120**, 945–951, DOI: 10.1016/j.ijbiomac.2018.09.011.

46 Z. Chen, Z. B. Zhang, J. Zeng, Z. J. Zhang, S. Ma, C. M. Tang and J. Q. Xu, Preparation of polyethyleneimine-modified chitosan/Ce-UIO-66 composite hydrogel for the adsorption of methyl orange, *Carbohydr. Polym.*, 2023, **299**, 120079, DOI: 10.1016/j.carbpol.2022.120079.

47 R. E. K. Billah, Y. Abdellaoui, Z. Anfar, G. Giácoman-Vallejos, M. Agunaou and A. Soufiane, Synthesis and Characterization of Chitosan/Fluorapatite Composites for the Removal of Cr (VI) from Aqueous Solutions and Optimized Parameters, *Water, Air, Soil Pollut.*, 2020, **231**, 163, DOI: 10.1007/s11270-020-04535-9.

48 V. Pitpisutkul and J. Prachayawarakorn, Hydroxypropyl methylcellulose/carboxymethyl starch/zinc oxide porous nanocomposite films for wound dressing application, *Carbohydr. Polym.*, 2022, **298**, 120082, DOI: 10.1016/j.carbpol.2022.120082.

49 K. Dharmalingam and R. Anandalakshmi, Fabrication, characterization and drug loading efficiency of citric acid

 © 2026 The Author(s). Published by the Royal Society of Chemistry

Open Access Article. Published on 04 February 2026. Downloaded on 2/26/2026 3:16:51 PM.
This article is licensed under a Creative Commons Attribution-NonCommercial 3.0 Unported Licence.

crosslinked NaCMC-HPMC hydrogel films for wound healing drug delivery applications, *Int. J. Biol. Macromol.*, 2019, **134**, 815–829, DOI: 10.1016/J.IJBIOMAC.2019.05.027.

50 P. Kanmani and J. W. Rhim, Properties and characterization of bionanocomposite films prepared with various biopolymers and ZnO nanoparticles, *Carbohydr. Polym.*, 2014, **106**, 190–199, DOI: 10.1016/J.CARBPOL.2014.02.007.

51 C. Tang, Y. Xu, K. Zhou, Y. Xie, Y. Ma, C. Li, F. Xu, H. Zhou and B. Xu, Mechanism behind the deterioration in gel properties of collagen gel induced by high-temperature treatments: A molecular perspective, *Food Res. Int.*, 2023, **171**, 112985, DOI: 10.1016/J.FOODRES.2023.112985.

52 Y. S. R. Elnaggar, M. Zewail, E. M. Salem, W. Y. Alghonemy, N. M. Ahmed, O. M. Abdelfatah, R. A. Hanafy and M. A. Moustafa, Development and Appraisal of Luteolin-Loaded Nanohyaluosomes as a Sustainable Tissue Engineering Nanotherapy for Treatment of Periodontitis: Biochemical and Biological Investigations, *J. Drug Delivery Sci. Technol.*, 2026, 107957.

53 N. Saikia, Inorganic-based nanoparticles and biomaterials as biocompatible scaffolds for regenerative medicine and tissue engineering: Current advances and trends of development, *Inorganics*, 2024, **12**, 292.

54 K. S. Almulhim, M. R. Syed, N. Alqahtani, M. Alamoudi, M. Khan, S. Z. Ahmed and A. S. Khan, Bioactive inorganic materials for dental applications: a narrative review, *Materials*, 2022, **15**, 6864.

55 E. De Carli, A. Lagou, S. Kiliaridis and B. J. Denes, Mandibular condyle changes in rats with unilateral masticatory function, *Orthod. Craniofac. Res.*, 2023, **26**, 37–45.

56 P. D. Rohmaniar, R. P. Rahayu, I. D. A. B. Narmada, N. Sa'adah and D. Andriani, Effect of Diabetes Mellitus on Each Phase of Tooth Extraction Socket Healing, *J. Int. Dent. Med. Res.*, 2024, **17**, 429–434.

57 S. Yang, Y. Li, C. Liu, Y. Wu, Z. Wan and D. Shen, Pathogenesis and treatment of wound healing in patients with diabetes after tooth extraction, *Front. Endocrinol.*, 2022, **13**, 949535.

58 X. Wang, R. Li and H. Zhao, Enhancing angiogenesis: Innovative drug delivery systems to facilitate diabetic wound healing, *Biomed. Pharmacother.*, 2024, **170**, 116035.

59 G. Gazal, Management of an emergency tooth extraction in diabetic patients on the dental chair, *Saudi Dent. J.*, 2020, **32**, 1–6.

60 S. A. Antar, N. A. Ashour, M. Sharaky, M. Khattab, N. A. Ashour, R. T. Zaid, E. J. Roh, A. Elkamhawy and A. A. Al-Karmalawy, Diabetes mellitus: Classification, mediators, and complications; A gate to identify potential targets for the development of new effective treatments, *Biomed. Pharmacother.*, 2023, **168**, 115734.

61 R. Ruze, T. Liu, X. Zou, J. Song, Y. Chen, R. Xu, X. Yin and Q. Xu, Obesity and type 2 diabetes mellitus: connections in epidemiology, pathogenesis, and treatments, *Front. Endocrinol.*, 2023, **14**, 1161521.

62 G. J. P. L. de Oliveira, L. A. Fontanari, J. A. C. de Souza, R. Spin-Neto, C. N. Elias, E. Marcantonio Junior and S. R. P. Orrico, Fluoride-modified implant surfaces improves osseointegration in the tibias of rats with induced diabetes, *Braz. Dent. J.*, 2023, **34**, 43–52.

63 L. Borkowski, A. Przekora, A. Belcarz, K. Palka, G. Jozefaciuk, T. Lübek, M. Jojczuk, A. Nogalski and G. Ginalska, Fluorapatite ceramics for bone tissue regeneration: Synthesis, characterization and assessment of biomedical potential, *Mater. Sci. Eng., C*, 2020, **116**, 111211, DOI: 10.1016/J.MSEC.2020.111211.

64 S. Liu, H. Zhou, H. Liu, H. Ji, W. Fei and E. Luo, Fluorine-contained hydroxyapatite suppresses bone resorption through inhibiting osteoclasts differentiation and function in vitro and in vivo, *Cell Proliferation*, 2019, **52**, e12613.

65 H. T. Shiu, P. C. Leung and C. H. Ko, The roles of cellular and molecular components of a hematoma at early stage of bone healing, *J. Tissue Eng. Regener. Med.*, 2018, **12**, e1911–e1925.

66 M. Wang, G. Jiang, H. Yang and X. Jin, Computational models of bone fracture healing and applications: A review, *Biomed. Eng.*, 2024, **69**, 219–239.

67 H. Zeng, X. Li, F. Xie, L. Teng and H. Chen, Dextran-coated fluorapatite nanorods doped with lanthanides in labelling and directing osteogenic differentiation of bone marrow mesenchymal stem cells, *J. Mater. Chem. B*, 2014, **2**, 3609–3617.

68 S. Seyedmajidi and M. Seyedmajidi, Fluorapatite: A Review of Synthesis, Properties and Medical Applications vs Hydroxyapatite, *Iran. J. Mater. Sci. Eng.*, 2022, **19**.

69 R. Mascarenhas, S. Hegde and N. Manaktala, Chitosan nanoparticle applications in dentistry: A sustainable biopolymer, *Front. Chem.*, 2024, **12**, 1362482.

70 M. Souto-Lopes, L. Grenho, Y. Manrique, M. M. Dias, J. C. B. Lopes, M. H. Fernandes, F. J. Monteiro and C. L. Salgado, Bone regeneration driven by a nano-hydroxyapatite/chitosan composite bioaerogel for periodontal regeneration, *Front. Bioeng. Biotechnol.*, 2024, **12**, 1355950.

71 Z. Li, C. Zhang, L. Wang, Q. Zhang, Y. Dong, X. Sha, B. Wang, Z. Zhu, W. Wang and Y. Wang, Chitooligosaccharides promote diabetic wound healing by mediating fibroblast proliferation and migration, *Sci. Rep.*, 2025, **15**, 556.

72 R. Elimelech, N. Khoury, T. Tamari, I. Blumenfeld, Z. Gutmacher and H. Zigdon-Giladi, Use of transforming growth factor-β loaded onto β-tricalcium phosphate scaffold in a bone regeneration rat calvaria model, *Clin. Implant Dent. Relat. Res.*, 2019, **21**, 593–601.

73 B. M. Chesnutt, Y. Yuan, K. Buddington, W. O. Haggard and J. D. Bumgardner, Composite chitosan/nano-hydroxyapatite scaffolds induce osteocalcin production by osteoblasts in vitro and support bone formation in vivo, *Tissue Eng., Part A*, 2009, **15**, 2571–2579.

74 N. N. Patlataya, I. N. Bolshakov, V. A. Khorzhevskii, A. A. Levenets, N. N. Medvedeva, M. A. Cherkashina, M. M. Nikolaenko, E. I. Ryaboshapko and A. E. Dmitrienko, Morphological Reconstruction of a Critical-Sized Bone Defect in the Maxillofacial Region Using Modified Chitosan in Rats with Sub-Compensated Type I Diabetes Mellitus, *Polymers*, 2023, **15**, 4337.